# High-throughput investigation of ferrite growth kinetics in graded ternary Fe-C-X alloys

Imed-Eddine Benrabah, H.P Van Landeghem, Frédéric Bonnet, Benoit Denand, Guillaume Geandier, Alexis Deschamps

# High-throughput investigation of ferrite growth kinetics in graded ternary Fe-C-X alloys

I.-E. Benrabah[a], H.P Van Landeghem[b], F. Bonnet[c], B. Denand[d], G. Geandier[d], A. Deschamps[b]

[a] *Department of Materials Science and Engineering, McMaster University, Hamilton, Ontario L8S 4L7, Canada.*
[b] *Univ. Grenoble Alpes, CNRS, Grenoble INP, SIMAP, F-38000 Grenoble, France.*
[c] *ArcelorMittal Research, F-57280 Maizières-lès-Metz, France.*
[d] *Institut Jean Lamour, UMR CNRS-Université de Lorraine 7198, F-54000 Nancy, France.*

---

**Abstract**

The composition dependence of ferrite growth kinetics in Fe-C-X ternary alloyed steels, where X=Ni, Mn, Mo, Cr, Si, was investigated using a high-throughput approach. Compositionally graded samples were subjected to in situ time- and space-resolved X-ray diffraction during intercritical annealing. To this end, diffusion couples were created between a binary Fe-C and different Fe-C-X alloys, using hot uniaxial compression and high temperature diffusion treatments. In-situ high-energy X-ray diffraction experiments were performed to collect ferrite growth kinetics along the composition gradient of the diffusion couples. A large dataset describing the austenite-to-ferrite phase transformation kinetics was generated using a very limited number of experiments. This dataset of unprecedented size was compared to the kinetics predicted by the classical local-equilibrium (LE) and para-equilibrium (PE) models as well as a modified version of the three-jump solute drag (SD) model, which accounts for the different interactions between the elements present at the austenite/ferrite interface. The comparison showed that both LE and PE models fail to capture the effect of both composition and temperature on the kinetics of ferrite growth for the different Fe-C-X systems. The SD model calculations matched experimental transformation kinetics at all investigated temperatures and over almost all the investigated composition ranges of Si, Cr, Mn, Ni, and Mo.

*Keywords:* Combinatorial metallurgy, Graded steels, High-throughput

methodology, Ferrite growth kinetics, Solute drag

## 1. Introduction

Low-alloy steels are a broad family of materials encompassing alloys critical to numerous industrial fields, including energy and transport, which are of particular relevance in the current environmental context. Further enhancing their properties is necessary to reach higher performance in those applications. This can be achieved by adding controlled amounts of specific alloying elements and tailoring the processing route accordingly. These parameters determine the obtained microstructure, which imparts the material its final properties [1, 2, 3]. Knowledge of how the composition/thermomechanical schedule couple controls phase transformations, including their kinetics, is a prerequisite to the optimal design and processing of low-alloy steel grades. Among all phase transformations in steels, the austenite-to-ferrite transformation is probably that of widest application and correspondingly has been the object of a very large research interest [1, 4, 5].

Under industrial conditions, the austenite-to-ferrite transformation occurs with negligible redistribution of the slow-diffusing substitutional elements (e.g. Al, Si, Cr, Mn, Ni, Mo...) [1, 6, 7, 8, 9, 10]. Modeling the kinetics of this transformation mode is of great interest due to the crucial role of the transformation in achieving the properties of many modern grades. Simple models such as paraequilibrium (PE) or local equilibrium with negligible partitioning (LENP) were proven to diverge from experimental findings for many temperature/composition combinations [4, 6, 7, 9, 10, 11, 12, 13, 14, 15]. More elaborate models showed greater success in matching experimental observations but usually require more input parameters than the already available thermodynamic data of the bulk phases,such as the mixed mode models [16, 17, 18, 19] and the solute drag (SD) models. The later models account for the energy dissipation originating from the interaction of the substitutional solute with the moving interface [20, 21, 22, 23, 24, 25]. Quantifying this dissipation requires a comprehensive description of the interface thermodynamics. Both Cahn [20] and Hillert [21] proposed a solute drag based approach to describe phase transformations kinetics. Different solute drag based numerical models were developed to describe the austenite-to-ferrite growth kinetics. One should note here that these models are relevant only for cases where carbon is the main controlling mechanism for ferrite growth and energy

dissipation related to the intrinsic mobility of the interface can be neglected. The solute drag models [10, 24, 26, 27] require the input of two main fitting parameters, namely the binding energy ($E_b$), which represents the interaction between the solute element and iron at the interface and the trans-interface diffusion coefficient of the solute element. Moreover, the mutual interactions between the co-existing solute elements as well as their interaction with carbon can affect the segregation tendency (and thus the binding energy) of solute elements. Recently, the three-jump SD model, originally proposed by Zurob et al. [26], was adapted to account for the different interactions between the existing elements at the interface, and to take into account the high amount of carbon segregated at the transformation interface, which was measured experimentally in several studies. The model predictions showed good agreement with ferrite precipitation kinetics in several Fe-C-X ternary alloys [28]. In this new version of the SD model, only the Fe-X interaction parameter at the interface was used as a fitting parameter. Assessing the dependency on composition and temperature of these interaction parameters requires laborious experimental work. Such investigations were conducted by Qiu et al. [29, 30] and Zurob et al. [26] using decarburization experiments for different Fe-C-X systems (X :Mn, Ni, Cr, Mo, Si and Co), and lately using precipitation experiments [28] for different Fe-C-X (X : Ni, Mn, Cr and Mo) alloys. Results showed that experimental data for several compositions and temperatures can be described with constant interaction parameters with the three-jump SD model. Despite this extensive work, the experimental data available covers only a few alloy compositions and temperatures, which makes it difficult to assess the robustness of the modelling strategy and consequently its applicability outside the tested conditions. As such, it remains sub optimal to extract the interfacial thermodynamic information required by SD models and to assess the robustness of such models outside the few compositions where the model has been fitted to experimental data. Additionally, little quantitative data exists in the industrially relevant conditions of ferrite precipitation, since most quantitative work has been carried out during decarburization experiments where the interface velocity is much slower [29, 31, 32, 33, 34, 35].

Historically, the effect of composition on phase transformations has been assessed by processing and characterizing discrete sets of alloys, which, due to the time-consuming and resource intensive nature of the task, were usually quite restricted. High throughput experimental techniques represent a solution to rapidly explore a large set of parameters and accelerate materials development [36, 37, 38, 39, 40, 41]. Compositionally graded alloys have been used to

investigate the composition-dependence of microstructures [42, 43, 44, 45, 31, 46, 47]. X-Ray diffraction provides several attractive features for high-throughput screening such as in situ monitoring of microstructural evolution and space resolved characterization, well suited to couple with compositionally graded alloys [42, 43, 48, 49]. In a recent paper, we have reported a complete combinatorial methodology that allows mapping the austenite-to-ferrite transformation kinetics as a function of composition in steels [50]. This technique consists in performing in situ, time- and space-resolved synchrotron X-ray diffraction measurements on compositionally graded specimens.

In the present work, this combinatorial methodology was applied for high throughput mapping of ferrite growth kinetics in ternary Fe-C-X systems, where X stands for the substitutional species Ni, Mn, Mo, Cr, Si, aiming at obtaining an unprecedentedly comprehensive dataset of ferrite precipitation kinetics in a broad alloy composition range. These experimental results are then used to compare with PE, LENP and three-jump SD model calculations. The obtained results will also allow identifying if constant physical parameters of the SD models are capable of describing the compositional dependency of ferrite precipitation kinetics.

## 2. Experimental procedure

### *2.1. Materials*

The initial composition of as received samples used to make the graded materials is shown in table 1. These samples were cast at ArcelorMittal, Maizières-les-Metz, France, hot rolled and homogenized at 1200 °C for 18h.

Table 1: Chemical compositions (wt. %) of the different alloys used to make diffusion couples, realized by Spark-OES method.

| Composition %wt | C | Si | Mn | Mo | Cr | Ni | Al | Other alloying elements |
|---|---|---|---|---|---|---|---|---|
| Fe-C | 0.27 | 0.024 | 0.004 | <0.002 | <0.002 | <0.002 | 0.003 | <0.002 |
| Fe-C-Ni | 0.29 | 0.03 | 0.005 | <0.002 | <0.002 | 1.07 | 0.004 | <0.002 |
| Fe-C-Mn | 0.28 | 0.03 | 0.98 | <0.002 | <0.002 | <0.002 | 0.003 | <0.002 |
| Fe-C-Mo | 0.27 | 0.02 | 0.004 | 0.21 | <0.002 | <0.002 | 0.004 | <0.002 |
| Fe-C-Cr | 0.28 | 0.028 | 0.005 | <0.002 | 0.96 | <0.002 | 0.003 | <0.002 |
| Fe-C-Si | 0.27 | 1.2 | 0.004 | <0.002 | <0.002 | <0.002 | 0.006 | <0.002 |

Using the base compositions listed in table 1, blocks of the binary Fe-C alloy were joined to a matching block of each ternary Fe-C-X alloy to create diffusion couples containing a composition gradient of substitutional element X.

*2.2. Fabrication of diffusion couples*

The fabrication method for the compositionally graded samples is detailed in [50]. It can be summarized as follows :

1. Creating solid-state bonds between different alloys using uniaxial hot compression.
2. Generating compositional gradients at high temperature by diffusion process in a decarburization atmosphere.
3. Re-introducing the desired carbon content using a carburizing treatment.
4. Grain size refinement using cyclic austenitization/quenching treatments and cold rolling.

The composition profiles across the diffusion couples were characterized using electron probe micro-analysis (EPMA). Measurements were carried out using a CAMECA SX50 electron microprobe with an accelerating voltage of 15 kV and a probe current of 900 nA. To have a good measurement accuracy, carbon standards with different carbon contents were used to calibrate the C K$\alpha$ intensity as a function of carbon content. A linear relationship was assumed between carbon content and the measured intensity [51, 47, 50].

*2.3. High energy X-ray diffraction experiments*

Ferrite fraction evolution was measured using high energy X-ray diffraction technique. Measurements were carried at the beamline P21.1 in PETRA III at DESY synchrotron in Hamburg (Germany). A high energy beam of 82 keV ($\lambda = 0.1512$ Å) was used to work in transmission mode. The beam size of 1 x 0.08 mm$^2$ was chosen to maximize the number of diffracting grains as well as to obtain a good spatial resolution. Debye Sherrer rings were collected using a 2D detector ( VAREX 4343CT) placed at 1 m of the sample with an acquisition rate of 10 Hz [50].

Samples with a cylindrical shape (30 mm length and 3 mm diameter) were machined from the diffusion couples. Heat treatments were achieved in a lamp furnace as that allows rotating the samples during heat treatments and thus increasing the number of grains in the diffracted volume [52, 50]. The temperature gradient along the diffusion couples was estimated for each sample [50]. This thermal gradient was taken into account in phase transformation modeling. Samples were translated along the composition gradient using a vertical motor with a maximum speed of 1 mm.s$^{-1}$ to collect diffraction patterns at different compositions.Diffraction patterns were recorded continuously

during the heat treatments. Considering the present configuration, diffraction patterns were recorded every 6 to 22 s (depending on the gradient length and the analyzed position) for each composition along the gradient.

The heat treated diffusion couples were austenitized at 910 °C (or 980 °C for Si containing diffusion couples) for 30 s, quenched to an inter-critical temperature (730, 750 or 775 °C) and held at this temperature for 15 min before being quenched to room temperature. In the results provided further below, only the ferrite growth kinetics data corresponding to the isothermal hold is shown for clarity. The collected Debye Sherrer rings were integrated to 1D diffraction patterns using pyFAI [53]. Rietveld's refinement (using FullProf [54]) was used to analyze the integrated patterns and extract the volume fractions of austenite and ferrite. For small fractions (<5%), an integration method was used to calculate ferrite and austenite fractions as described in Appendix A.

## 3. Phase transformation modeling

Three models were compared to experimental measured ferrite growth kinetics : LE, PE and a new version of the 'three-jump solute drag (SD)' model [28]. Local equilibrium (LE) and para-equilibrium (PE) models were carried using TCFE9 and MOB2 databases of the ThermoCalc software [55]. TThe adopted geometry of both the parent austenite and the nucleated ferrite can have an effect on the calculated kinetics as shown in [56, 19]. In the current study, ferrite was assumed to nucleate on the surface of a spherical austenite grain and grow by diffusion into the spherical grain. The parent austenite grain size was estimated using optical microscopy and used as input parameter for modeling. The effect of nucleation on the overall transformation was neglected in the present study. Nucleation was assumed to be complete at the very early stages of the transformation. This was supported by the optical micrographs of interrupted transformation after 30 seconds at 750 °C (Figure S1 in the supplementary material), showing that ferrite nucleates on the whole austenite grain boundary suggesting site saturation.

Solute drag calculations were carried using a modified version of the three-jump model proposed by Zurob et al. [26]. The details of this modified model are described in [28]. The 'three jump' model assumes that during the austenite-to-ferrite transformation, the substitutional elements diffuse through a thick discrete interface using three jumps characterized by their

diffusion coefficients. The first jump uses the diffusion coefficient in ferrite (D$\alpha$), the third one uses that in austenite ( D$\gamma$) and the second one uses the geometrical average of D$\alpha$ and D$\gamma$ [26]. The most important parameter in the model is the interaction parameter between substitutional element X (a substitutional element) and Fe at the interface, which describes its segregation at the interface. This parameter is expressed using the $L_{Fe,X:Va;0}$ interaction parameter in the ThermoCalc database. In the present version of the model, only this parameter was used as a fitting parameter. For simplicity, this parameter will be referred to as the Fe-X interaction parameter. Note that this parameter can be related to the binding energy as explained in [28]. Here both the interaction parameter Fe-X and its corresponding binding energy will be indicated. The binding energy can also be derived from solute segregation measurements using APT technique, and can be estimated from the enrichment factor ($K_{max}$) using equation 1 [20], where $x_{X,max}$ and $x_{X,0}$ are the maximal X segregation at the interface and the bulk content. $\Delta E$ is the half difference between chemical potentials of element X in austenite and ferrite. $E_0$ is here called the effective binding energy as it expresses the segregation energy of the element in the presence of all other elements such as carbon in the present case.

$$K_{max} = \frac{x_{X,max}}{x_{X,0}} = \exp(\frac{E_0 - \Delta E}{RT}) \quad (1)$$

One objective of this study is to investigate the dependency of the fitting parameter (Fe-X) on composition and temperature. In our earlier report [28], the present version of the SD model was used to calculate ferrite growth kinetics in different Fe-C-X systems (X :Mn, Ni, Mo and Cr) with constant compositions and at different temperatures. The Fe-X interaction parameters that provided the best description of the experimental data can be found in Table 7 of ref [28]. In the present contribution, these fitting parameters will be used as a starting test for the SD modeling of the different Fe-X-C graded alloys, with the objective to test the robustness of the model and to assess the sensitivity of the Fe-X interaction parameter to composition.

## 4. Results

The studied diffusion couples are summarized in table 2 as well as the austenitization temperature and the isothermal holding temperatures. Figure S2 in supplementary material shows an example of the obtained composition

Table 2: Summary of the investigated diffusion couples with their austenitization and isothermal holding temperatures. The measured composition gradient lengths as well as the carbon content, the temperature and the grain size measured along the gradient are indicated.

| Diffusion couple | $T_\gamma$ | $T_{iso}$ | Gradient length (mm) | Carbon content (wt. %) | Temperature gradient (°C/mm) | Grain size ($\mu$m) [±10] |
|---|---|---|---|---|---|---|
| Fe-C/Fe-C-Ni | 910°C | 730°C<br>750°C<br>775°C | 6 | 0.22 | 1.6 | 50 |
| Fe-C/Fe-C-Mn | 910°C | 730°C<br>750°C | 3 | 0.22 | 3.3 | 50 @ 730°C<br>70 @ 750°C |
| Fe-C/Fe-C-Si | 980°C | 730°C<br>750°C<br>775°C | 11 | 0.18 - 0.24 | 0.55 | 20 - 30 |
| Fe-C/Fe-C-Mo | 910°C | 730°C<br>750°C<br>780°C | 1.5 | 0.5 | 2 | 40 @ 730°C - 750°C<br>65 @ 780°C |
| Fe-C/Fe-C-Cr | 910°C | 750°C | 6.5 | 0.2 - 0.22 | 1.5 | 55 |

profiles, measured using electron probe micro-analysis, in a diffusion couple created between Fe-C and Fe-C-1Ni alloys. As it can be seen from Fig.S2 in supplementary material, the generated nickel concentration varies from 0 % to 1 % along of 6 mm. The exact length of the composition gradient differs from couple to couple depending on the diffusing element, but the order of magnitude remains the a few mm. Table 2 summarizes the composition gradient length for each diffusion couple. A constant carbon content of 0.22 % was measured across the nickel diffusion couple. One should note that for some diffusion couples, a gradient of carbon content was recorded along the X element gradient (e.g. for the Fe-C/Fe-C-Si diffusion couple). This gradient was taken into account for modeling. The other important parameters for the modeling are the initial grain size and the exact temperature. These parameters are shown in table 2 as well.

### *4.1. Fe-C-Ni system*

The measured ferrite fraction evolution as a function of time and nickel content, at 730 °C, 750 °C and 775 °C are shown in figure 1-a, -b and -c. The results for 730 °C (Fig. 1-a and 2-a) were already shown in our previous report [50]. These results are shown here for comparing with other temperatures. Given the 80 $\mu$m beam size in the direction of the composition gradient, each curve shown in figure 1 corresponds to a given nickel content with a maximum of nickel composition variation of 0.018 %. Results show a decrease of ferrite growth kinetics as well as the ferrite fraction reached at the plateau

with increasing nickel content and increasing temperature. The present example illustrates the efficiency of the present combinatorial methodology to provide extensive databases using a limited number of experiments (one sample per temperature).The effect of nickel on ferrite growth kinetics is more pronounced at higher temperature. This effect is illustrated in Fig. 1-d, which compares the ferrite fraction reached at the end of the isothermal holding for the three temperatures as a function of nickel composition. The final fraction decreases with increasing nickel content and increasing temperature.

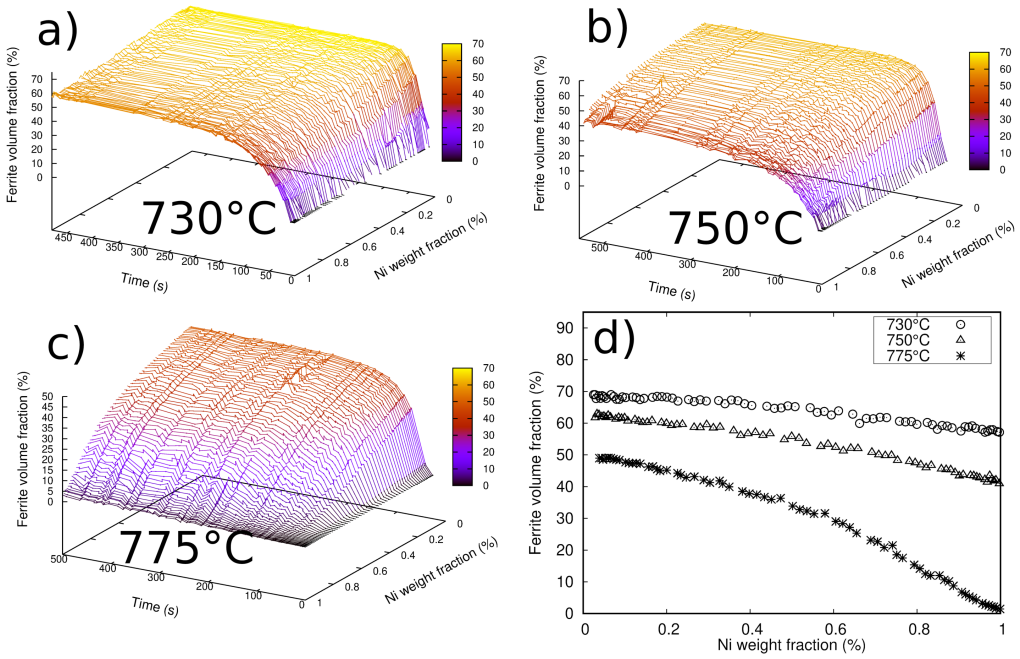


Figure 1: Ferrite fraction measured using HEXRD as a function of time and nickel composition along the Fe-C-Ni diffusion couple during isothermal hold at : a) 730°C (reproduced with permission from [50]), b) 750°C and c) 775°C. (Heatmaps showing the same data in a 2D plot are presented in figure S3 of the supplymentary materials). d) Ferrite fractions from HEXRD experiments along the gradient of the Fe-C-Ni diffusion couple at the end of the isothermal hold (15 min) at 730°C (black circles), 750°C (blue circles) and 775°C (red circles).

The recorded final ferrite fractions using HEXRD will be now compared with the ones obtained using LE, PE and SD calculations. The isothermal sections of the Fe-C-Ni phase diagram at 730°C, 750°C and 775°C, calculated using the TCFE9 database of ThermoCalc are illustrated in Fig.S4 in supplementary

material, showing the possible growth modes along the composition range of the diffusion couple. At the three temperatures, the whole composition gradient is located below the zero partition line where both LENP and PE are theoretically possible transformation modes. At 775°C, the 1%Ni side of the gradient is at the limit of the zero partition line.

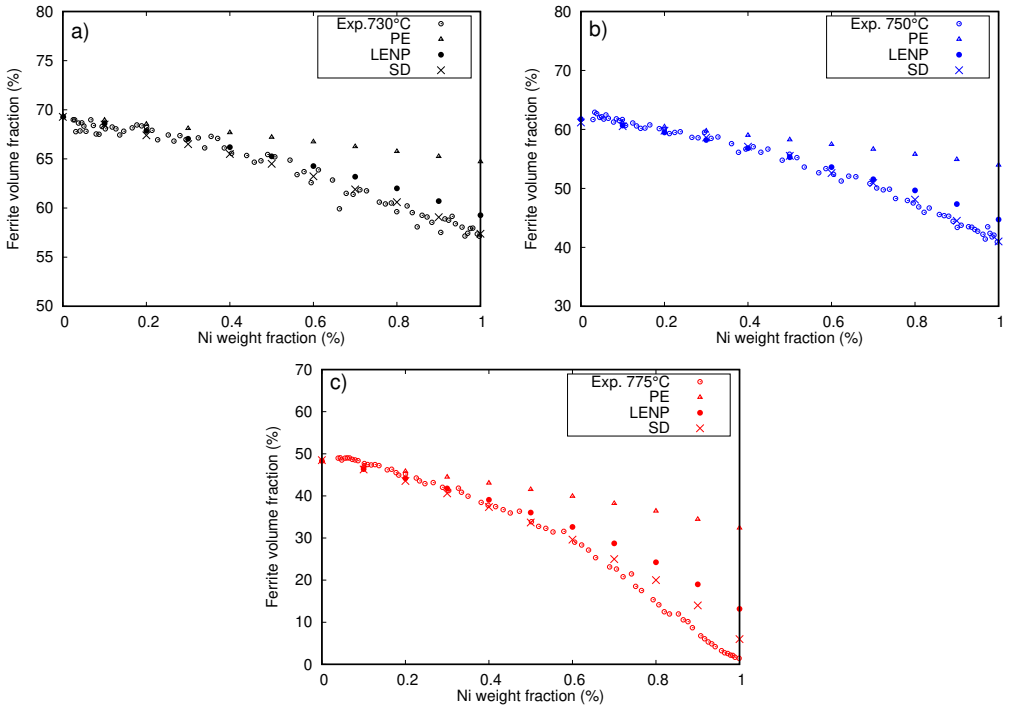


Figure 2: Comparison between the ferrite fractions measured after 900 s (open circles) and the predictions of paraequilibrium (triangles), local equilibrium with negligible partitioning (filled circles) and solute drag (crosses) models as a function of nickel content at : a) 730°C (reproduced with permission from [50]), b) 750°C and c) 775°C

First, the ferrite fractions reached at the end of the isothermal hold are compared with the predicted values using the different models as function of nickel composition as illustrated in figure 2-a, b and c at 730°C, 750°C and 775°C, respectively. For the three temperatures, PE fails to predict the final fraction evolution as function of nickel content. The gap between the measurements and the predicted final fraction increases with nickel content and temperature. A better but not perfect agreement is obtained between the measured fractions and the calculated ones using the LE model. At

730°C and 750°C, the LE model successfully predicts the measured final fractions up to 0.6 % Ni. At 775°C, the divergence between the model predictions and measurements starts at 0.4 % Ni. A very good agreement was obtained between the experimental measured final ferrite fractions and the predictions of solute drag modeling at the two temperatures 730°C and 750°C. It has to be emphasized that the same Fe-Ni interaction parameter was used to model ferrite growth kinetics over the whole nickel composition range for both temperatures, this value being slightly adjusted between the two temperatures (-11.7 $kJ.mol^{-1}$ and -11.8 $kJ.mol^{-1}$ at 730°C and 750°C, respectively). The calculated binding energy under para-equilibrium conditions was -6.5 $kJ.mol^{-1}$ for the whole gradient of nickel composition and at the two temperatures 730°C and 750°C. At 775°C, good agreement was obtained between experiments and the predictions of solute drag model up to 0.7%.wt nickel content using the same binding energy -6.5 $kJ.mol^{-1}$, corresponding to a Fe-Ni interaction parameter of -11.9 $kJ.mol^{-1}$. At higher nickel contents, the calculated ferrite fractions are slightly higher than the measured ones.

In a second step, the full experimental kinetics obtained by HEXRD has been compared to those calculated using the LE, PE and SD models. Figure 3 presents a map of ferrite fraction as function of time and nickel content, which gives an overall picture of the ferrite growth kinetics, as obtained by HEXRD at 730°C and by calculation using the different models. It is clear from these heat maps that both PE and LE fail to predict the experimental kinetics dependency on nickel content. The divergence between the measured kinetics and the calculated ones is more noticeable at high nickel contents. Overall, solute-drag-based calculations succeeded to describe the measured ferrite growth kinetics better than both PE and LE over the entire investigated composition range.

More quantitatively, the model predictions and experimental results can be compared for a given nickel composition and temperature as shown in figure 4 for two chosen nickel compositions (0.5Ni and 1Ni) at different temperatures. In all cases, the PE predicted kinetics are faster than the measured ones. The LE predicted kinetics are faster than the measured ones at 730°C and 775°C for both compositions. At 750°C, the predicted kinetics using the LE model is in good agreement with the measurements at low nickel compositions (0.5%) but faster than the measured kinetics at high nickel contents (1%). Results from SD calculations show a better agreement with experimental observations than both PE and LENP in all considered

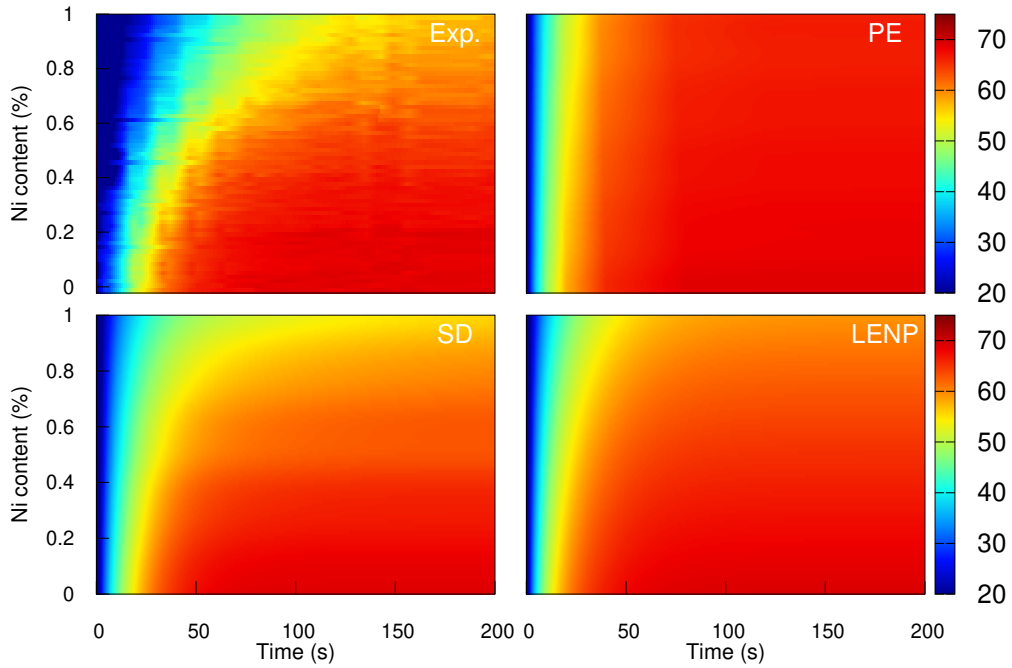


Figure 3: Heat maps illustrating ferrite volume fraction evolution as a function of time and nickel composition at 730°C, either as measured using high-energy X-ray diffraction measurements (Exp.) or as modeled using solute drag (SD) calculations, paraequilibrium (PE) and local equilibrium negligible partitioning (LENP) models.

conditions. One can however notice that the SD predicted kinetics are faster than the measured ones at 730°C.

### *4.2. Fe-C-Mn system*

The evolution of the measured ferrite fraction at 730°C and 750°C are shown in figure 5. The isothermal sections of the Fe-C-Mn phase diagrams at 730°C and 750°C are shown in Fig.S6 in supplementary material. At both temperatures, the studied composition range is located below the zero partition line where both LENP and PE are possible growth modes.

Figure 6 compares the measured final ferrite fractions reached at the plateau (at the end of the isothermal holding i.e. after 15 min) with the predicted values using the different models as function of manganese composition at 730°C and 750°C, respectively. For both temperatures, the PE model fails

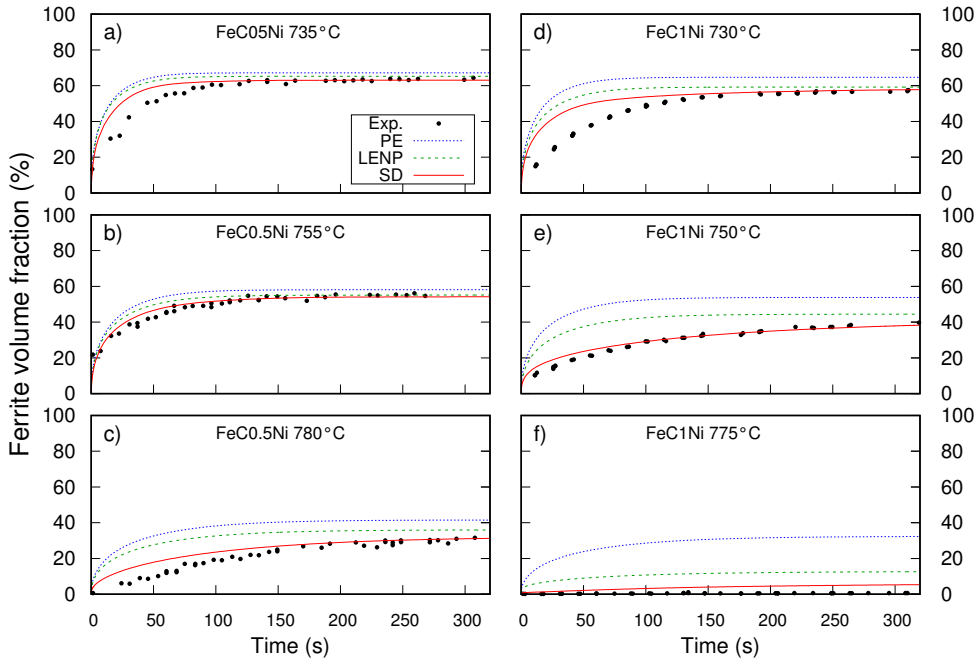


Figure 4: HEXRD-measured ferrite growth kinetics for different compositions of the Fe-C-Ni diffusion couple during the isothermal holding for the two compositions : Fe-0.22C-0.5Ni (%wt.) at : a) 735°C, b) 755°C and c) 780°C. and Fe-0.22C-1Ni (%wt.) at : d) 730°C, e) 750°C and f) 775°C. The calculated kinetics using paraequilibrium (PE), local equilibrium negligible partitioning (LENP) and solute drag (SD) models are shown for the different compositions. The difference in data resolution between the different plots is due to the difference in time resolution of each composition along the diffusion couple. The temperature difference between the 0.5Ni and 1Ni is attributed to the temperature gradient along the diffusion couple.

to predict the measured ferrite fraction when manganese content increases. The discrepancy between the predicted PE fraction and the measured one increases with increasing manganese content and with temperature. On the other hand, the LE model describes well the final ferrite fraction formed at 750°C for the whole composition range and up to 0.6% for the 730°C case. At higher manganese contents, the LE predicted final ferrite fraction is lower than the measured value (5% lower at 0.9wt% of Mn). The SD succeeded in predicting the ferrite fractions reached at the end of the isothermal holding for the whole range of manganese composition and at both temperatures (Fig.

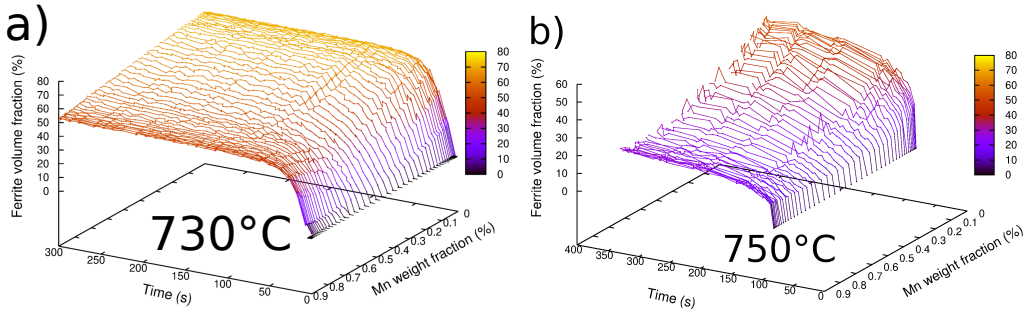


Figure 5: HEXRD-measured ferrite fraction evolution as a function of time and manganese composition along the Fe-C-Mn diffusion couple during the isothermal holding at a) 730°C and b) 750°C. (Heatmaps showing the same data in a 2D plot are presented in figure S5 of the supplymentary materials)

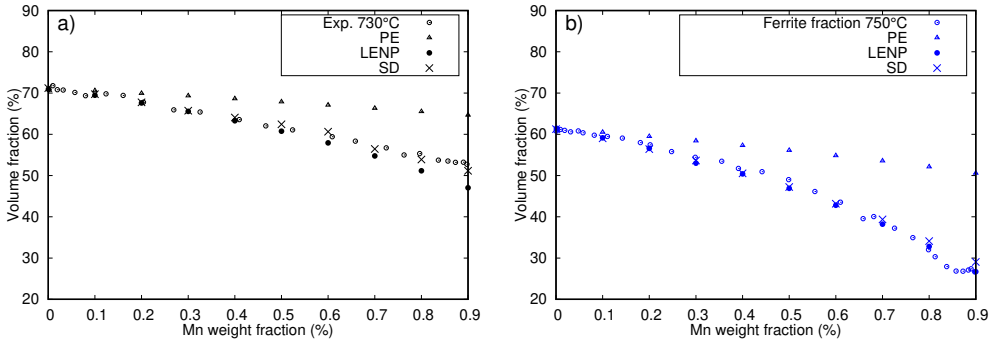


Figure 6: Comparison between the measured final ferrite fractions (open circles) and the predictions of paraequilibrium (PE) (triangles), LE (filled dots) and solute drag (crosses) models as function of manganese content at : a) 730°C and b) 750°C.

6). The Fe-Mn interaction parameter used for solute drag modeling was -1.4 $kJ.mol^{-1}$ at 730°C and -1.7 $kJ.mol^{-1}$ at 750°C corresponding to a binding energy calculated at the para-equilibrium conditions of +1.5 $kJ.mol^{-1}$ for both temperatures.

The measured ferrite growth kinetics using HEXRD experiments are compared with the predictions of the different models for a series of compositions in figure 7. The kinetics predicted by PE are faster than the experimental ones in all conditions. Figure 7 shows that the LE mode successfully describes the measured growth kinetics at 750°C. A small deviation is noticed for high manganese contents at 730°C. The comparison between the measured growth kinetics and the calculated ones using PE and LE models indicates that the

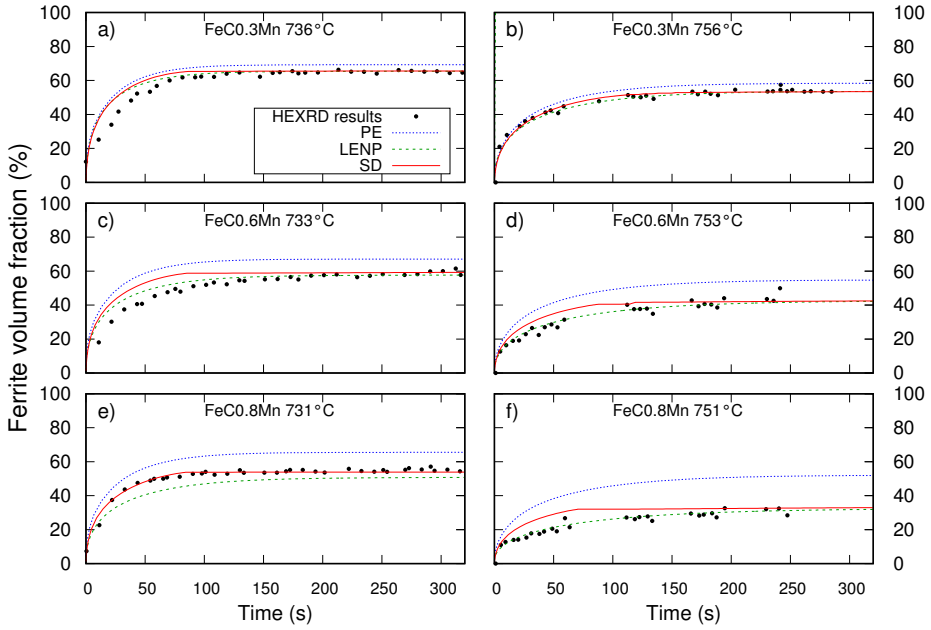


Figure 7: Experimental ferrite growth kinetics measured using HEXRD experiments for different compositions of the Fe-C-Mn diffusion couple during the isothermal holding for the three compositions: Fe-0.22C-03Mn (%wt.) at : a) 736°C and b) 756°C. Fe-0.22C-0.6Mn (%wt.) at : c) 733°C and d) 753°C. Fe-0.22C-0.8Mn (%wt.) at : e) 731°C and f) 751°C. The calculated kinetics using paraequilibrium (PE), local equilibrium negligible partitioning (LENP) and solute drag (SD) models are shown for the different compositions.

interfacial conditions during austenite to ferrite phase transformation in the Fe-C-Mn system could be described using the LENP model, at least under the studied conditions ( 0 to 0.9 %Mn at 730°C and 750°C). The solute drag calculations show also a good agreement between the predicted ferrite growth kinetics and the measured ones using HEXRD as shown in figure 7. One should mention here that, at 750°C, the calculated kinetics using the LE model are in better agreement with the experimental measurements compared to those calculated using the SD model.

### *4.3. Fe-C-Si system*

The measured ferrite fraction as a function of time and silicon composition is plotted in figure 8 for the three temperatures 730°C, 750°C and 775°C. Results show that ferrite growth kinetics as well as the reached final fraction

at the plateau increase with increasing silicon content. It has to be mentioned here that this variation of the final fraction is influenced by the important carbon gradient as measured using EPMA (Fig. S7 in supplementary material) as well as the temperature gradient.

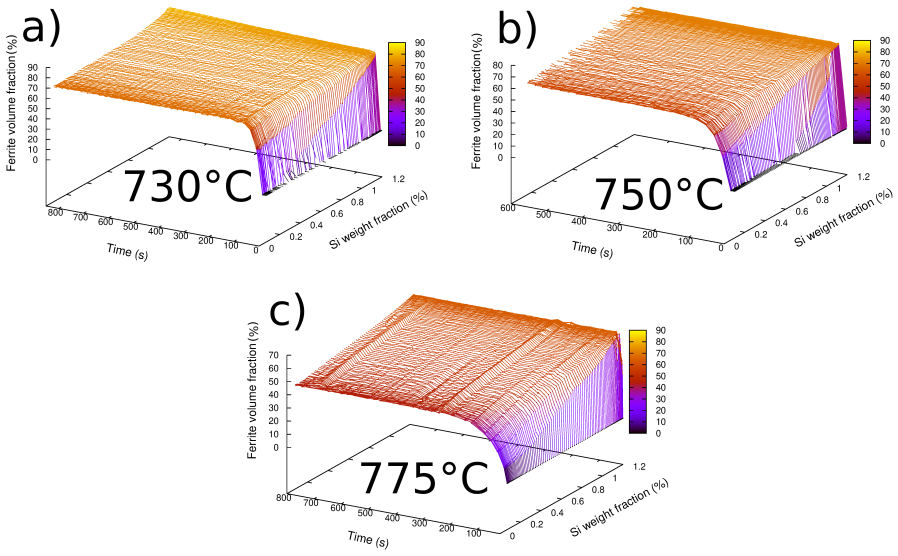


Figure 8: Evolution of ferrite fraction measured using HEXRD as a function of time and silicon composition along the Fe-C-Si diffusion couple during the isothermal holding at : a) 730°C b) 750°C and c) 775°C. (Heatmaps showing the same data in a 2D plot are presented in figure S8 of the supplymentary materials)

The isothermal sections of the Fe-C-Si phase diagram are illustrated in figure S9 in supplementary material showing the studied gradient of silicon composition at the three temperatures. For all the studied composition and temperature conditions, both PE and LENP are possible growth modes.

The comparison between the predicted final fractions using LE, PE and SD models and the obtained results using HEXRD experiments is shown in figure 9. For the three temperatures, the final ferrite fraction is overestimated by both PE and LE models and the gap between measurements and model predictions becomes larger with increasing silicon content and increasing temperature. The measured final fractions are in good agreement with the solute drag results at the three temperatures and for the whole studied composition range. Table 3 summarizes the Fe-Si interaction parameters at the interface that gave the best agreement of the experimental results as

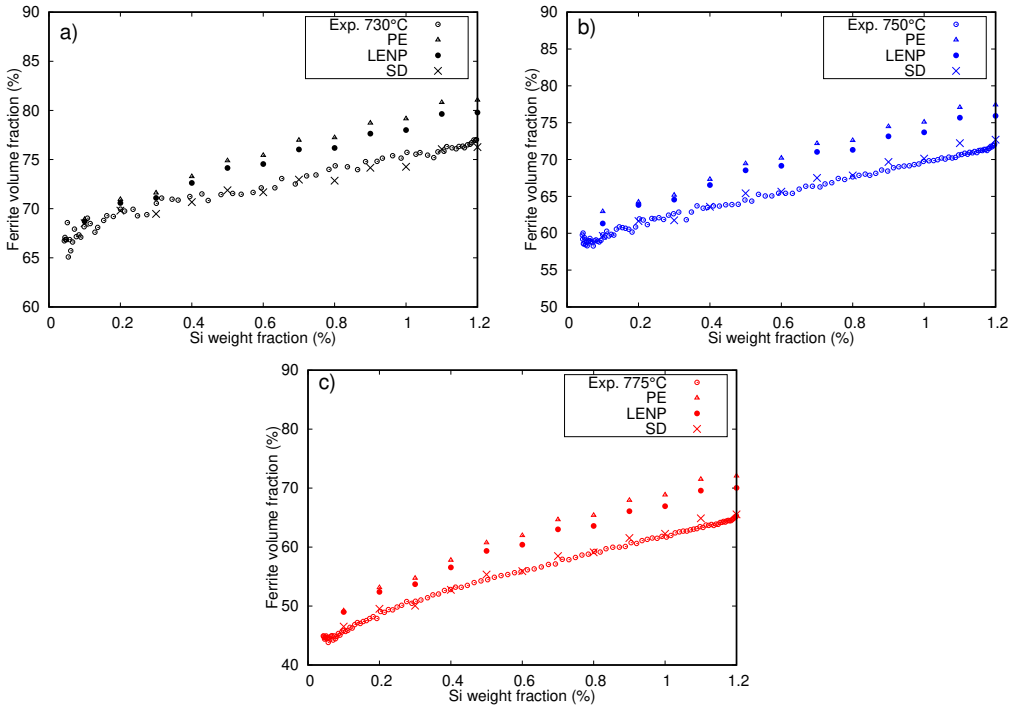


Figure 9: Comparison between the measured final ferrite fractions (open circles) and the predictions of paraequilibrium (PE) (triangles), local equilibrium with negligible partitioning (filled dots) and solute drag (crosses) models as function of silicon content at: a) 730°C, b) 750°C and c) 775°C

well as the calculated binding energies ($E_b$) of silicon under para-equilibrium conditions. Unlike the previous studied systems systems, the Fe-Si interaction parameter shows a dependency on temperature. At each temperature, the same fitting parameter was used for the whole range of silicon composition (0-1.2 %). The magnitude of the Fe-Si interaction parameters and the corresponding binding energies decrease with increasing temperature.

Figure 10 compares the measured ferrite growth kinetics and the modeled ones, for two silicon compositions (0.5Si and 1Si (wt.%)) at the three temperatures 730°C, 750°C and 775°C. The ferrite growth kinetics as well as the final fractions predicted using both LE and PE models are quite similar. For all the shown composition and temperature conditions, the measured kinetics are slower than both PE and LE calculations, indicating different interfacial conditions from both classical models during ferrite growth in the Fe-C-Si

Table 3: The Fe-Si interaction parameter $L_{Fe,Si:Va}$ and the corresponding binding energies (calculated under para-equilibrium conditions) used in the solute drag modeling at the three different temperatures.

| T(°C) | $L_{Fe,Si:Va}$ $(kJ.mol^{-1})$ | $E_b$ $(kJ.mol^{-1})$ |
|---|---|---|
| 730 | -105.5 | -20 |
| 750 | -100 | -15 |
| 775 | -96 | -12 |

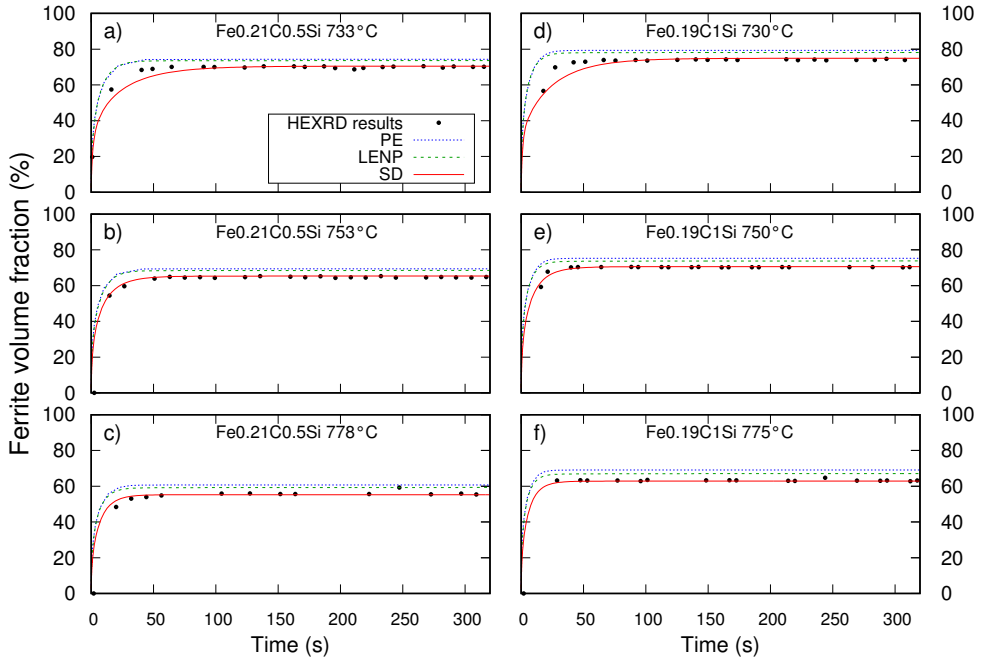


Figure 10: Experimental ferrite growth kinetics measured using HEXRD experiments in the Fe-C-Si diffusion couple during the isothermal holding for the two compositions : Fe-0.21C-0.5Si (%wt.) at : a) 733°C, b) 753°C and c) 778°C. and Fe-0.19C-1Si (%wt.) at : d) 730°C, e) 750°C and f) 775°C. The calculated kinetics using paraequilibrium (PE), local equilibrium negligible partitioning (LENP) and solute drag (SD) models are shown for the different compositions.

system. Moreover, the results contradicts the assumption of a transition between PE and LE conditions during the transformation since the measured kinetics is slower than both PE and LE predicted ones. On the other hand,

the solute drag predicted kinetics are in good agreement with the measured ones for all the considered conditions as shown in figure 10.

### *4.4. Fe-C-Mo system*

Figure 11 illustrates ferrite fraction evolution as function of molybdenum content during the isothermal holding for the three temperatures 730°C, 750°C and 780°C, respectively.

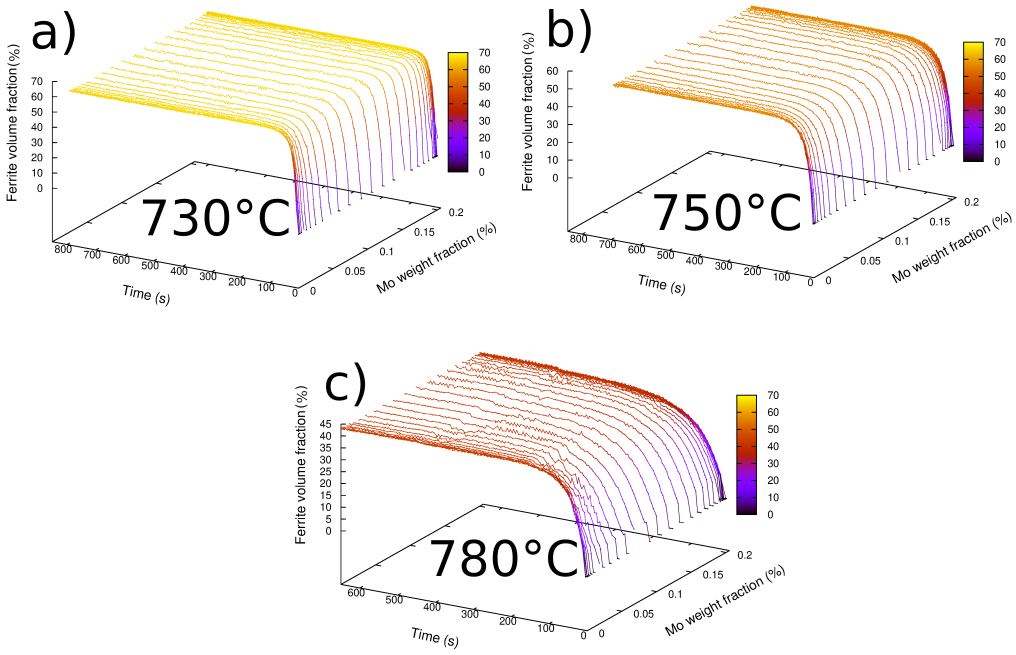


Figure 11: Evolution of ferrite fraction measured using HEXRD as a function of time and molybdenum composition along the Fe-C-Mo diffusion couple during the isothermal holding at : a) 730°C b) 750°C and c) 780°C. (Heatmaps showing the same data in a 2D plot are presented in figure S10 of the supplymentary materials)

The isothermal sections of the Fe-C-Mo phase diagrams are shown in Fig.S11 in supplementary material illustrating the studied composition gradient. For the three temperatures, both LENP and PE are possible growth modes. Moreover, under the considered conditions (composition and temperatures) the equilibrium tie-lines are almost horizontal (as shown by green lines in figure S11 in supplementary material) and thus coincide with the para-equilibrium tie-lines. Consequently, the predicted kinetics using LE (LENP) or PE should be similar.

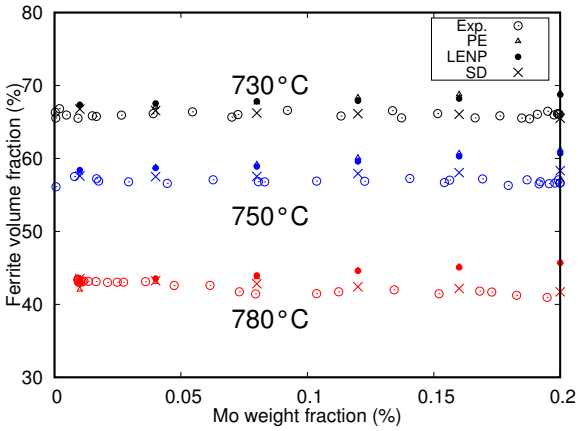


Figure 12: Comparison between the measured final ferrite fractions (open circles) and the predictions of paraequilibrium (triangles), local equilibrium with negligible partitioning (filled dots) and solute drag (crosses) models as function of molybdenum content at 730°C (black), 750°C (blue) and 780°C (red).

Figure 12 compares the final fractions reached at the end of the isothermal holding with the predicted values using LE, PE and SD models as a function of molybdenum composition and temperature. It is interesting to note that the experimentally measured final fractions are approximately constant across the molybdenum composition gradient. This could also be impacted by the small temperature gradient along the samples ($\sim$3°C). For the three studied temperatures, the predicted LE/PE final fraction is slightly higher than the measured one and the difference increases with increasing molybdenum content and with decreasing temperature. The SD predicted final fractions are in good agreement with the experimental ones. The measured kinetics are compared with the LE/PE predicted ones for two molybdenum compositions (0.08% and 0.2% wt.) at different temperatures in figures 13-a to 13-f. Again, the solute drag model gave the best description of both the final fractions and the ferrite kinetics over the whole range of molybdenum compositions and at the three temperatures.

The Fe-Mo interaction parameters that gave the best fit of the experimental data were, -7.2 $kJ.mol^{-1}$, -7.5 $kJ.mol^{-1}$ and -8 $kJ.mol^{-1}$ at 730°C, 750°C and 780°C, respectively. The same Fe-Mo interaction parameter was used for the whole range of composition at each temperature. Using these parameters, the corresponding binding energy calculated under para-equilibrium conditions was -15 $kJ.mol^{-1}$ for the three temperatures and for all molybdenum compositions.

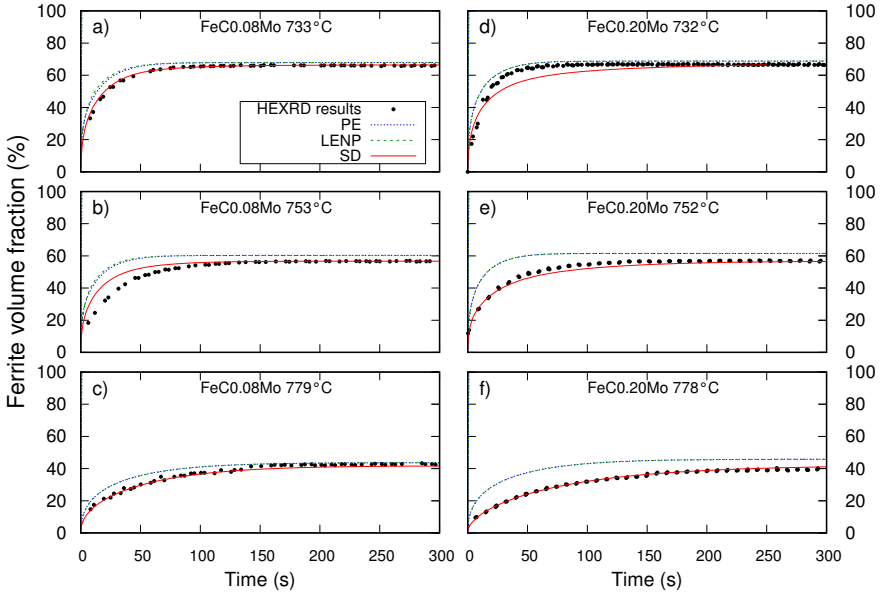


Figure 13: Experimental ferrite growth kinetics measured using HEXRD experiments in the Fe-C-Mo diffusion couple during the isothermal hold for the two compositions : Fe-0.25C-0.08Mo (%wt.) at : a) 733°C, b) 753°C and c) 779°C. and Fe-0.25C-0.2Mo (%wt.) at : d) 732°C, e) 7522°C and f) 778°C. The calculated kinetics using paraequilibrium (PE), local equilibrium negligible partitioning (LENP) and solute drag (SD) models are shown for the different compositions.

### *4.5. Fe-C-Cr system*

Figure 14-a shows the measured ferrite growth kinetics as a function of time and chromium content during the isothermal holding at 750°C. Figure 14-b shows the evolution of the ferrite fraction reached at the end of the isothermal holding as a function of chromium composition, measured using HEXRD as well as the predicted ones using PE, LE and SD models.

As shown by the isothermal section of the Fe-C-Cr phase diagram at 750°C presented in Fig.S13 in supplementary material, both LENP and PE are possible growth modes for the studied gradient of chromium. The predicted LE final fractions are in good agreement with the measured ones. A small deviation is observed between the measurements and the LE predictions at chromium contents higher than 0.6%. The measured ferrite fractions at the end of the isothermal holding are in good agreement with those predicted

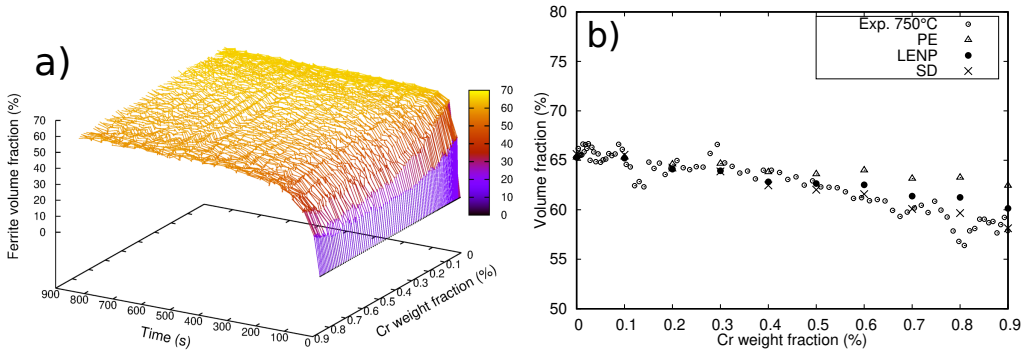


Figure 14: a) Evolution of ferrite fraction measured using HEXRD as a function of time and chromium composition along the Fe-C-Cr diffusion couple during the isothermal hold at 750°C. (Heatmaps showing the same data in a 2D plot are presented in figure S12 of the supplymentary materials). b) Comparison between the measured final ferrite fractions (open circles) and the predictions of paraequilibrium (triangles), local equilibrium with negligible partitioning (filled dots) and solute drag (crosses) models as function of chromium content at 750°C.

by the SD model. The best fit was obtained using a Fe-Cr interaction parameter + 5.3 $kJ.mol^{-1}$ corresponding to a binding energy calculated at para-equilibrium conditions of + 1.5 $kJ.mol^{-1}$.

Ferrite fraction evolution as function of time during the isothermal holding is shown in figure 15 for four different compositions. The measured kinetics is slower than both the predicted kinetics using PE and LE models and the difference increases with increasing chromium content. Although the predicted final fractions are in good agreement with the LE predictions, the growth kinetics are overestimated by the model. This discrepancy between the predicted PE/LE and the measured kinetics indicates again the presence of a possible additional energy dissipation due to SD effect. A better description of the measured ferrite growth kinetics was obtained using SD modeling compared to LE and PE models.

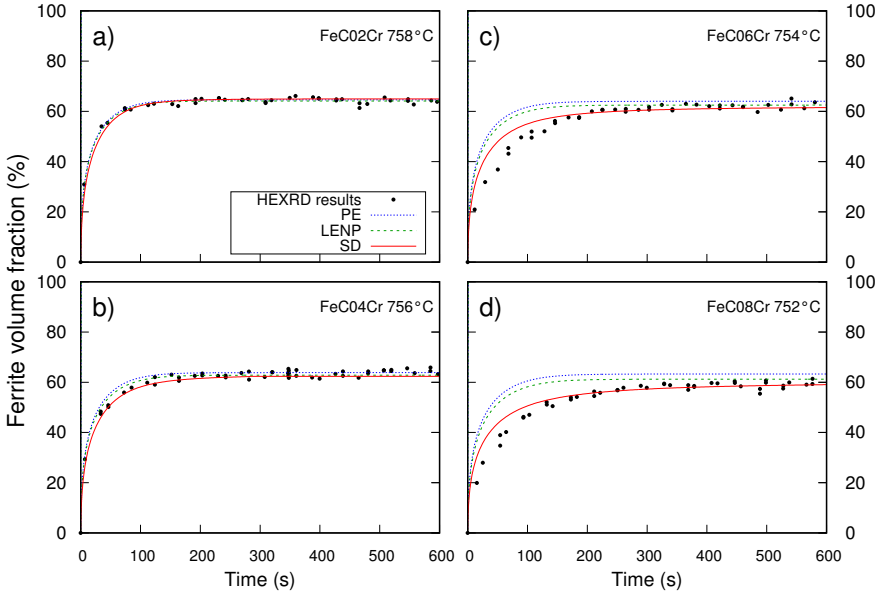


Figure 15: Experimental ferrite growth kinetics measured using HEXRD experiments in the Fe-C-Cr diffusion couple during the isothermal hold for four compositions: a) Fe-0.20C-0.2Cr (%wt.) at 758°C, b) Fe-0.21C-0.4Cr (%wt.) at 756°C, c) Fe-0.21C-0.6Cr (%wt.) at 754°C and d) Fe-0.20C-0.8Cr (%wt.) at 752°C. The calculated kinetics using paraequilibrium (PE), local equilibrium with negligeable partitioning (LENP) and solute drag (SD) models are shown for the different compositions.

## 5. Discussion

The extensive datasets presented above, afforded by the combinatorial methodology, enable, for the first time, the comparison of experimental ferrite precipitation kinetics to PE, LENP and SD over broad ranges of conditions in multiple systems. This comparison showed that ferrite growth kinetics cannot be described by the PE conditions under any of the studied conditions in most of the systems, where it systematically gave overestimated transformation rates. PE also failed to predict the final ferrite fractions in any of the present experimental conditions. Contrary to PE, LENP returned final ferrite fractions that were in reasonable agreement with experimental observations over the leaner parts of the composition gradients considered here for Cr, Mn, Ni and Mo. However, even in those favorable cases, LENP overestimated the transformation rates. For the Fe-C-Ni system, the measured ferrite growth

kinetics showed slower kinetics than the LE predictions. In addition, LENP calculations in the Fe-C-Si system showed considerable discrepancy with experimental observations for all temperatures and silicon content, both in terms of final ferrite fraction or transformation rate. Thus, these observations demonstrate that LENP is not a generally applicable model for partitionless ferrite growth either. This can be added as new evidence that the generally reported agreement between measured kinetics and the LE-predicted ones in some alloys as for example in the Fe-C-Ni [35, 31, 4] and Fe-C-Mn [26] systems cannot be generalized over the whole range of composition and temperature evaluated in the present work. Moreover, in the Fe-C-Si and Fe-C-Mo systems, the measured kinetics were slower than both LENP and PE. These results contradict the assumption of a transition from PE to LE conditions during the transformation [4, 57].

The solute drag model on the other hand was able to closely track the measured ferrite growth kinetics in the different Fe-C-X systems and over the whole range of studied conditions, using only one fitting parameter. The used fitting parameters were the same as used in the earlier study using samples with constant compositions. It is important to note that for all the studied system, the Fe-X fitting parameter showed no dependency on composition (in the studied conditions). However, this parameter seems to be sensitive to temperature as suggested by the Fe-C-Si system.

The energy dissipated by SD results from the interaction between the slow-diffusing substitutional elements and the moving interface. This effect is illustrated in figure 16-a showing the evolution of molybdenum content at the interface (only the second atomic plane of the interface is shown here) as a function of the interface velocity for the Fe-C-0.2%Mo alloy at the three temperatures 730°C,750°C and 780°C. At high interface velocities, the interface inherits a molybdenum content similar to that of the bulk. As the interface velocity decreases, molybdenum content at the interface increases due to solute drag effect. The maximum segregation is reached at slow interface velocities ($< 1e^{-10}$ m.s$^{-1}$) and its value increases with decreasing temperature. The resulting dissipated energy is also shown in Fig. 16-a. The dissipated energy increases with decreasing interface velocity and goes through a maximum, then decreases with the interface velocity. The maximum dissipated energy as a function of molybdenum content and temperature is presented in figure 16-b showing an increase of the maximum dissipated energy with increasing molybdenum content and with decreasing temperature. The effect of temperature is more noticeable at high molybdenum

content.

Hutchinson et al. [35] measured ferrite growth kinetics in Fe-C-Mo alloys using both precipitation and decarburization experiments. The authors showed that in both cases, the measured kinetics were slower than the LENP/PE kinetics. The authors attributed the observed retardation to the solute drag effect and estimated that the SD dissipated energy, as in the present calculations, increases with decreasing temperature.

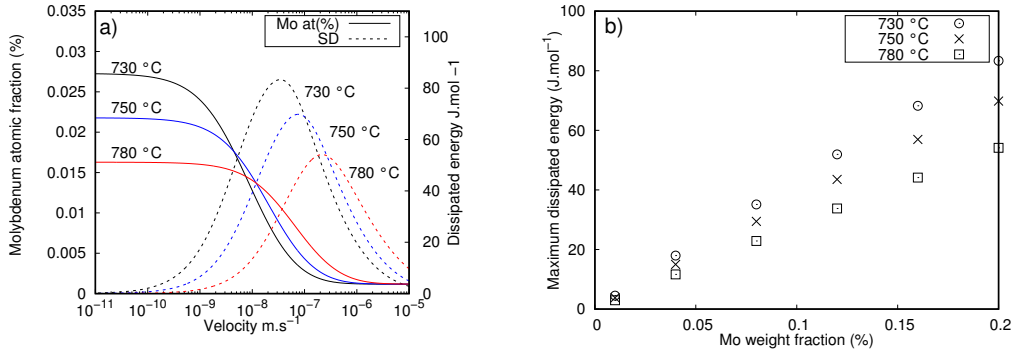


Figure 16: a) Molybdenum atomic fraction at the second atomic plane and the dissipated free energy due to molybdenum diffusion across the interface as function of the interface velocity for the Fe-0.25C-0.2Mo (%wt.) at the three temperatures, 730°C, 750°C and 780°C. b) Maximum dissipated energy as a function of molybdenum content for the three temperatures.

For a better illustration of the segregation behavior of molybdenum as a function of its bulk composition and temperature, the enrichment factor (Eq.1) is calculated at low interface velocities (approaching equilibrium conditions) and plotted in figure 17-a as a function of molybdenum content and for the three temperatures. The enrichment factor increases slightly with molybdenum content. The effect of composition is more pronounced at lower temperatures. On the other hand, the enrichment factor clearly decreases with increasing temperature.

The evolution of the effective binding energy (calculated using Eq.1) as a fucntion of molybdenum content is plotted in figure 17-b. Results show a clear increase of the effective binding energy with increasing temperature. The reported atom probe tomography (APT) measurements conducted by Van Landeghem et al.[58] on the Fe-0.55C-0.5Mo (wt.%) system showed a binding energy of -19 $kJ.mol^{-1}$ at 775°C, which is close to the calculated value in the present study (-20.5 $kJ.mol^{-1}$).

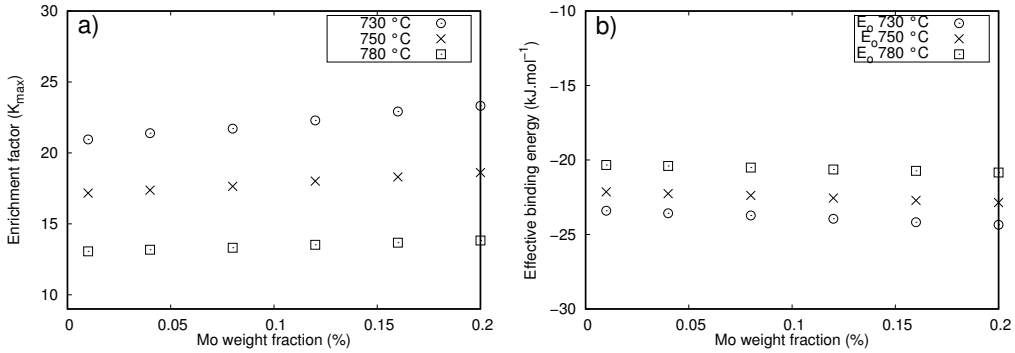


Figure 17: The enrichment factor $K_{max}$ (a) and the corresponding effective binding energy ($E_0$) (b) evolution as a function of molybdenum content for the three temperatures, 730°C, 750°C and 780°C.

Table 4: The enrichment ($K_{max}$) and the corresponding effective binding energy ($E_0$) calculated for the different Fe-C-X systems. The indicated values are mean values estimated over the gradient of composition. Fe-X ($L_{Fe,X:Va}$) interaction parameters that gave the best fit of the measured ferrite growth kinetics.

| Fe-C-X | Fe-C-Ni | | | Fe-C-Mn | | Fe-C-Si | | | Fe-C-Mo | | | Fe-C-Cr |
|---|---|---|---|---|---|---|---|---|---|---|---|---|
| T(°C) | 730 | 750 | 775 | 730 | 750 | 730 | 750 | 775 | 730 | 750 | 780 | 750 |
| $K_{max}$ | 3.5 (± 0.2) | 3.5 (± 0.2) | 3.5 (± 0.2) | 3 (± 0.2) | 2.8 (± 0.2) | 3.5 (± 1.5) | 2.5 (± 0.8) | 1.8 (± 0.6) | 22 (± 1) | 18 (± 1) | 13 (± 1) | 3.8 (± 0.2) |
| $E_0$ (kJ.mol$^{-1}$) | -7.2 (± 0.6) | -7.6 (± 0.6) | -8.2 (± 0.7) | -4.6 (± 0.4) | -4.2 (± 0.5) | -9 (± 3) | -7.5 (± 2.5) | -5.5 (± 1.5) | -23.5 (± 0.7) | -22.5 (± 0.3) | -20.5 (± 0.2) | -11.2 (± 0.5) |
| $L_{Fe,X:Va}$ ($kJ.mol^{-1}$) | -11.7 | -11.8 | -11.9 | -1.4 | -1.7 | -105.5 | -100 | -96 | -7.2 | -7.5 | -8 | +5.3 |

Using the same procedure, the enrichment factor and the corresponding effective binding energy were calculated for the different Fe-C-X systems as a function of X composition and at the different studied temperatures. The evolution of $K_{max}$ and $E_0$ as a function of composition are illustrated in Fig. S14 S15, S16 and S17 in supplementary material for the Fe-C-Ni, Fe-C-Mn, Fe-C-Si and Fe-C-Cr alloys, respectively. Table 4 summarizes the average values calculated over the composition range at each temperature. The enrichment factor of nickel is not much affected by temperature or composition. The dependency of the effective binding energy on composition and temperature is weak, -7.2 (± 0.6) $kJ.mol^{-1}$ , -7.6 (± 0.6) $kJ.mol^{-1}$ and -8.2 (±0.7) $kJ.mol^{-1}$ at 730°C, 750°C and 775°C, respectively. Atom probe measurements conducted on decarburized Fe-C-Ni alloys showed no significant Ni segregation at the austenite ferrite interface, contrarily to the high nickel segregation predicted by the present model ($K_{max}$ 3.5)[58]. The

effective binding energy of manganese increases slightly with temperature and it is not much affected by manganese content (in the studied range between 0 and 0.9%). Danoix et al. [59] assessed the effective binding energy of manganese to be -6 $kJ.mol^{-1}$ in a Fe-0.12C-2Mn (wt.%) alloy at 680°C. This value is comparable with the calculated one for the Fe-C-1%Mn at 730°C in the present study, i.e. -5 $kJ.mol^{-1}$. On the other hand, the effective binding energy of silicon shows a clear dependency on temperature and silicon content. One should note that this behavior is probably enhanced by the effect of the carbon gradient across the graded sample. Finally, the calculated effective binding energy for the chromium at 750°C is -11.2 ($\pm$ 0.5) $kJ.mol^{-1}$.

The effective binding energy calculated from the enrichment factor using Eq.1 is affected by other segregated elements, especially by the presence of carbon in the present case. To decorrelate the effect of carbon on the segregation energy of the different elements, the intrinsic segregation energy ($\Delta G^0$) was estimated using Guttmann's approach as explained in [28]. Results are plotted in Fig.18 along with the effective binding energies for the same X elements. Due to the repulsive interaction between nickel and carbon, the intrinsic segregation energy of this element is lower than its effective one. The calculated value is lower than the reported ones in the literature (-3 ($\pm$ 3) $kJ.mol^{-1}$) at ferrite grain boundaries [60] and at the lower limit of the reported ones ($>$ -7 $kJ.mol^{-1}$) at austenite grain boundaries [61]. For manganese, calculations show that this element segregates at the interface mainly due to the presence of carbon. This agrees with the experimental observations of Van Landeghem et al. [62]. The authors reported that manganese showed no segregation at the $\gamma/\alpha$ interface in the absence of carbon. The intrinsic segregation of manganese (-1.95 ($\pm$ 0.1) $kJ.mol^{-1}$ ) is higher than the reported theoretical values for manganese segregation at austenitic grain boundaries (-8 ($\pm$ 3) $kJ.mol^{-1}$) [61] or at ferrite grain boundaries (-5.5 $kJ.mol^{-1}$) [60].

Unlike manganeses, the segregation of silicon is diminished by the presence of carbon at the interface due to their repulsive interaction. The calculated intrinsic segregation energies of silicon are in good agreement with the reported values for austenite grain boundaries, -23 ($\pm$ 6 $kJ.mol^{-1}$) but lower than the reported ones for ferrite grain boundaries (-7 $kJ.mol^{-1}$). For molybdenum, the presence of carbon at the interface enhances its segregation as shown in Fig.18 The intrinsic segregation energy of molybdenum is estimated to -14.5 $kJ.mol^{-1}$ which is good agreement with the reported value in austenitic grain

boundaries (-15 +/-3 $kJ.mol^{-1}$) [61]. Finally, chromium segregation at the interface is mainly due to the presence of carbon and its intrinsic segregation energy is estimated to -1.9 $kJ.mol^{-1}$ at 750 °C. This value is higher than the reported values at austenite grain boundaries( -10 $kJ.mol^{-1}$ [61] ) and comparable to the reported ones at ferrite grain boundaries (0 $kJ.mol^{-1}$ [60]).

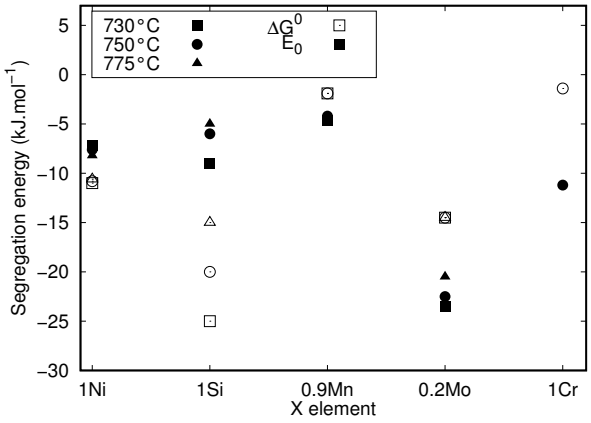


Figure 18: The effective binding energy $E_0$ (filled) and the intrinsic segregation energy $\Delta G^0$ (open) for the dffierent elements calculated at the three temperatures, 730°C (squares), 750°C (circles) and 775°C (triangles).

## 6. Conclusion

The effect of substitutional element contents on ferrite growth kinetics in ternary Fe-C-X systems (where X : Ni, Mn, Si, Mo, Cr) has been determined at different temperatures using a high-throughput, combinatorial methodology. The large dataset obtained in this study highlights the critical contribution of using HEXRD technique coupled with compositionally graded materials in accelerating the investigation of ferrite growth kinetics in ternary Fe-C-X systems. The obtained results were compared with the predictions of the PE and LE models as well as a modified version of the hree-jump SD model. For all the studied Fe-C-X systems, the PE model failed to predict the measured ferrite growth kinetics. Moreover, it was shown that the LE model cannot be used to fully describe ferrite growth kinetics for the whole substitutional composition gradient in the Fe-C-Ni and Fe-C-Mn systems, where it is generally reported that the LE model can be considered as a

natural state of ferrite precipitation [30]. It was also shown that, even in cases where the LE model predicted well the final ferrite fractions, it failed to describe the ferrite transformation kinetics. Additionally, the transformation rates observed in Fe-C-Mo and Fe-C-Si were consistently below both of those calculated using either PE or LENP, thus rejecting the hypothesis that the transformation proceeds with a transition from one mode to the other.

The SD model was also used to predict ferrite growth kinetics as a function of the solute content and temperature. The only fitting parameter was the Fe-X interaction parameter at the interface. Results from the SD model showed very good agreement between the measured ferrite growth kinetics and the calculated ones. For all the studied systems, the used Fe-X interaction parameters were independent from the X composition but showed a dependency on temperature as summarized in table 4. The calculated enrichment factors and the effective binding energies were in good agreement with the reported ones in literature, except for the Fe-C-Ni system, where the calculated segregations are higher than the experimentally measured ones.

**Acknowledgements**

The authors acknowledge DESY (Hamburg, Germany), a member of the Helmholtz Association HGF, for the provision of experimental facilities. HEXRD experiments were carried out at PETRA III and we would like to thank Dr. U. Lienert and Dr. Z. Hegedues for assistance in using beamline P21.2. Prof. H.S. Zurob is acknowledged for stimulating discussion and valuable input regarding solute drag modelling. Dr. Florence Robaut is acknowledged for her support with the EPMA measurements. This work was supported by the ANR (Agence Nationale de la Recherche [ANR-15-IDEX-02] and by MIAI@Grenoble Alpes [ANR-19-P3IA-0003].

## Appendix A. Numerical evaluation of low volume fractions

The low volume fractions ($<5\%$) observed in the early stages of the heat treatments are not well estimated using Rietveld refinement. In these cases, ferrite and austenite volume fractions were calculated by integrating the area of isolated peaks for both phases. The chosen peaks are (200), (211) and (321) for FCC-austenite and (200), (211) and (211) for BCC-ferrite. The background was estimated using a linear interpolation between the peak tails. The volume fraction of ferrite $f_\alpha$ was estimated using equation :

$$f_\alpha = \frac{\frac{1}{N}\sum_{i=1}^{N}\left(\frac{I_{\alpha,i}}{R_{\alpha,i}}\right)}{\frac{1}{N}\sum_{i=1}^{N}\left(\frac{I_{\alpha,i}}{R_{\alpha,i}}\right) + \frac{1}{M}\sum_{i=1}^{M}\left(\frac{I_{\gamma,i}}{R_{\gamma,i}}\right)} \tag{A.1}$$

where $(I_\gamma, i)$ and $(I_\alpha, i)$ are the integrated intensities for austenite and ferrite, respectively. N and M are ferrite and austenite reflection numbers, respectively. The index i refers to the h k l refection of interest. $R_{\gamma,i}$ and $R_{\alpha,i}$ are normalization factors for the austenite and ferrite peak intensities, respectively, extracted from the ICCD files (international centre for diffraction data).

## References


[1] Harry Bhadeshia and Robert Honeycombe. *Steels: Microstructure and Properties*. Elsevier, April 2011. Google-Books-ID: 6MtuBqok43MC.

[2] S. van der Zwaag. Kinetics of phase transformations in steels. In *Phase Transformations in Steels*, pages 126–156. Elsevier, 2012.

[3] M. Strangwood. Fundamentals of ferrite formation in steels. In *Phase Transformations in Steels*, pages 187–224. Elsevier, 2012.

[4] M. Gouné, F. Danoix, J. Ågren, Y. Bréchet, C.R. Hutchinson, M. Militzer, G. Purdy, S. van der Zwaag, and H. Zurob. Overview of the current issues in austenite to ferrite transformation and the role of migrating interfaces therein for low alloyed steels. *Materials Science and Engineering: R: Reports*, 92:1–38, June 2015.

[5] Matthias Militzer. Phase field modeling of microstructure evolution in steels. *Current Opinion in Solid State and Materials Science*, 15(3):106–115, 2011.

[6] H. K. D. H. Bhadeshia. Diffusional formation of ferrite in iron and its alloys. *Progress in Materials Science*, 29(4):321–386, January 1985.

[7] Masato Enomoto. Comparison of alloy element partition behavior and growth kinetics of proeutectoid ferrite in Fe-C-X alloys with diffusion growth theory. *ISIJ Int.*, 28(10):826–835, 1988.

[8] M ENOMOTO. Local Conditions at Moving a/g Boundaries of Proeutectoid Ferrite Transformation in Iron Alloys. *METALLURGICAL AND MATERIALS TRANSACTIONS A*, page 8.

[9] J. B. Gilmour, G. R. Purdy, and J. S. Kirkaldy. Partition of manganese during the proeutectoid ferrite transformation in steel. *Metallurgical Transactions*, 3(12):3213–3222, December 1972.

[10] K Oi, C Lux, and G.R Purdy. A study of the influence of Mn and Ni on the kinetics of the proeutectoid ferrite reaction in steels. *Acta Materialia*, 48(9):2147–2155, May 2000.

[11] A. Van der Ven and L. Delaey. Models for precipitate growth during the $\gamma \rightarrow \alpha + \gamma$ transformation in Fe-C and Fe-C-M alloys. *Progress in Materials Science*, 40(3):181–264, January 1996.

[12] Mats Hillert. Nature of local equilibrium at the interface in the growth of ferrite from alloyed austenite. *Scripta materialia*, 46(6):447–453, 2002.

[13] D. E. Coates. Diffusion-controlled precipitate growth in ternary systems I. *Metallurgical and Materials Transactions B*, 3(5):1203–1212, 1972.

[14] C. R. Hutchinson, A. Fuchsmann, and Y. Brechet. The diffusional formation of ferrite from austenite in Fe-C-Ni alloys. *Metallurgical and Materials Transactions A*, 35(4):1211–1221, April 2004.

[15] Goro Miyamoto and Tadashi Furuhara. Interaction of alloying elements with migrating ferrite/austenite interface. *Isij International*, 60(12):2942–2953, 2020.

[16] C. Bos and J. Sietsma. A mixed-mode model for partitioning phase transformations. *Scripta Materialia*, 57(12):1085–1088, December 2007.

[17] Ernst Gamsjäger. A note on the contact conditions at migrating interfaces. *Acta materialia*, 55(14):4823–4833, 2007.

[18] Ernst Gamsjäger. A concise derivation of the contact conditions at a migrating sharp interface. *Philosophical magazine letters*, 88(5):363–369, 2008.

[19] Ernst Gamsjäger, Robert E Werner, Wolfgang Schiller, and Bruno Buchmayr. Kinetics of the austenite-to-f errite phase transformation–simulations and experiments. *steel research international*, 85(2):131–142, 2014.

[20] John W Cahn. The impurity-drag effect in grain boundary motion. *Acta metallurgica*, 10(9):789–798, 1962.

[21] Mats Hillert and Bo Sundman. A treatment of the solute drag on moving grain boundaries and phase interfaces in binary alloys. *Acta Metallurgica*, 24(8):731–743, August 1976.

[22] G. R. Purdy and Y. J. M. Brechet. A solute drag treatment of the effects of alloying elements on the rate of the proeutectoid ferrite transformation in steels. *Acta metallurgica et materialia*, 43(10):3763–3774, 1995.

[23] F. Fazeli and M. Militzer. Application of solute drag theory to model ferrite formation in multiphase steels. *Metallurgical and Materials Transactions A*, 36(6):1395–1405, June 2005.

[24] Hao Chen and Sybrand van der Zwaag. A general mixed-mode model for the austenite-to-ferrite transformation kinetics in Fe–C–M alloys. *Acta Materialia*, 72:1–12, June 2014.

[25] J. Odqvist, Mats Hillert, and John \AAgren. Effect of alloying elements on the $\gamma$ to $\alpha$ transformation in steel. I. *Acta Materialia*, 50(12):3213–3227, 2002.

[26] H. S. Zurob, D. Panahi, C. R. Hutchinson, Y. Brechet, and G. R. Purdy. Self-Consistent Model for Planar Ferrite Growth in Fe-C-X Alloys. *Metallurgical and Materials Transactions A*, 44(8):3456–3471, August 2013.

[27] M. Enomoto. Influence of solute drag on the growth of proeutectoid ferrite in Fe–C–Mn alloy. *Acta materialia*, 47(13):3533–3540, 1999.

[28] I-E Benrabah, HP Van Landeghem, F Bonnet, B Denand, G Geandier, and A Deschamps. Solute drag modeling for ferrite growth kinetics during precipitation experiments. *Acta Materialia*, page 117364, 2021.

[29] C. Qiu, H. S. Zurob, D. Panahi, Y. J. M. Brechet, G. R. Purdy, and C. R. Hutchinson. Quantifying the Solute Drag Effect on Ferrite Growth in Fe-C-X Alloys Using Controlled Decarburization Experiments. *Metallurgical and Materials Transactions A*, 44(8):3472–3483, August 2013.

[30] Cong Qiu. *The 'Solute-Drag' Effect on Migrating Interfaces during Solid-State Phase Transformations*. PhD thesis.

[31] A. Phillion, H. W. Zurob, C. R. Hutchinson, H. Guo, D. V. Malakhov, J. Nakano, and G. R. Purdy. Studies of the influence of alloying elements on the growth of ferrite from austenite under decarburization conditions: Fe-C-Nl alloys. *Metallurgical and Materials Transactions A*, 35(4):1237–1242, April 2004.

[32] H.S. Zurob, C.R. Hutchinson, Y. Bréchet, H. Seyedrezai, and G.R. Purdy. Kinetic transitions during non-partitioned ferrite growth in Fe–C–X alloys. *Acta Materialia*, 57(9):2781–2792, May 2009.

[33] A. Béché, H.S. Zurob, and C.R. Hutchinson. Quantifying the Solute Drag Effect of Cr on Ferrite Growth Using Controlled Decarburization Experiments. *Metallurgical and Materials Transactions A*, 38(12):2950–2955, November 2007.

[34] C. Qiu, H.S. Zurob, and C.R. Hutchinson. The coupled solute drag effect during ferrite growth in Fe–C–Mn–Si alloys using controlled decarburization. *Acta Materialia*, 100:333–343, November 2015.

[35] C. R. Hutchinson, H. S. Zurob, and Y. Bréchet. The growth of ferrite in Fe-C-X alloys: The role of thermodynamics, diffusion, and interfacial conditions. *Metallurgical and Materials Transactions A*, 37(6):1711–1720, June 2006.

[36] Alexis Deschamps, Franck Tancret, Imed-Eddine Benrabah, Frédéric De Geuser, and Hugo P Van Landeghem. Combinatorial approaches for the design of metallic alloys. *Comptes Rendus Physique*, 19(8):737–754, 2018.

[37] D. Raabe, H. Springer, I. Gutierrez-Urrutia, F. Roters, M. Bausch, J. B. Seol, M. Koyama, P. P. Choi, and K. Tsuzaki. Alloy Design,

Combinatorial Synthesis, and Microstructure–Property Relations for Low-Density Fe-Mn-Al-C Austenitic Steels. *JOM*, 66(9):1845–1856, September 2014.

[38] J Zhao. Combinatorial approaches as effective tools in the study of phase diagrams and composition–structure–property relationships. *Progress in Materials Science*, 51(5):557–631, July 2006.

[39] Ji-Cheng Zhao, Xuan Zheng, and David G. Cahill. Thermal conductivity mapping of the Ni–Al system and the beta-NiAl phase in the Ni–Al–Cr system. *Scripta Materialia*, 66(11):935–938, June 2012.

[40] Ji-Cheng Zhao. A combinatorial approach for efficient mapping of phase diagrams and properties. *Journal of Materials Research*, 16(6):1565–1578, 2001.

[41] J.-C. Zhao, Xuan Zheng, and David G. Cahill. High-throughput diffusion multiples. *Materials Today*, 8(10):28–37, October 2005.

[42] F. De Geuser, M.J. Styles, C.R. Hutchinson, and A. Deschamps. High-throughput in-situ characterization and modeling of precipitation kinetics in compositionally graded alloys. *Acta Materialia*, 101:1–9, December 2015.

[43] E. Gumbmann, F. De Geuser, A. Deschamps, W. Lefebvre, F. Robaut, and C. Sigli. A combinatorial approach for studying the effect of Mg concentration on precipitation in an Al–Cu–Li alloy. *Scripta Materialia*, 110:44–47, January 2016.

[44] R.K.W. Marceau, C. Qiu, S.P. Ringer, and C.R. Hutchinson. A study of the composition dependence of the rapid hardening phenomenon in Al–Cu–Mg alloys using diffusion couples. *Materials Science and Engineering: A*, 546:153–161, June 2012.

[45] C Hutchinson. A novel experimental approach to identifying kinetic transitions in solid state phase transformations. *Scripta Materialia*, 50(2):285–290, January 2004.

[46] A Borgenstam and M Hillert. Massive transformation in the Fe–Ni system. *Acta Materialia*, 48(11):2765–2775, June 2000.

[47] Imed-Eddine Benrabah, Hugo Paul Van Landeghem, Frédéric Bonnet, Florence Robaut, and Alexis Deschamps. Use of space-resolved in-situ high energy x-ray diffraction for the characterization of the compositional dependence of the austenite-to-ferrite transformation kinetics in steels. *Quantum Beam Science*, 4(1):1, 2020.

[48] J. M. Gregoire, D. G. Van Campen, C. E. Miller, R. J. R. Jones, S. K. Suram, and A. Mehta. High-throughput synchrotron X-ray diffraction for combinatorial phase mapping. *J Synchrotron Rad*, 21(6):1262–1268, November 2014.

[49] R. Ivanov, A. Deschamps, and F. De Geuser. High throughput evaluation of the effect of Mg concentration on natural ageing of Al-Cu-Li-(Mg) alloys. *Scripta Materialia*, 150:156–159, June 2018.

[50] Imed-Eddine Benrabah, Frédéric Bonnet, Benoît Denand, Alexis Deschamps, Guillaume Geandier, and Hugo P Van Landeghem. High-throughput compositional mapping of phase transformation kinetics in low-alloy steel. *Applied Materials Today*, 23:100997, 2021.

[51] Florence Robaut, Alexandre Crisci, Madeleine Durand-Charre, and Danielle Jouanne. Practical aspects of carbon content determination in carburized steels by epma. *Microscopy and Microanalysis*, 12(4):331–334, 2006.

[52] Benoit Denand, Moukrane Dehmas, Elisabeth Gautier, Christophe Bonnet, Guillaume Geandier, and Jean-Pierre Sarteaux. PORTABLE ANALYSIS OVEN FOR RADIATION LINE, April 2019.

[53] J Kieffer, V Valls, N Blanc, and C Hennig. New tools for calibrating diffraction setups. *Journal of synchrotron radiation*, 27(2):558–566, 2020.

[54] Juan Rodriguez-Carvajal. Fullprof: a program for rietveld refinement and pattern matching analysis. In *satellite meeting on powder diffraction of the XV congress of the IUCr*, volume 127. Toulouse, 1990.

[55] Jan-Olof Andersson, Thomas Helander, Lars Höglund, Pingfang Shi, and Bo Sundman. Thermo-calc & dictra, computational tools for materials science. *Calphad*, 26(2):273–312, 2002.

[56] M Militzer, MG Mecozzi, J Sietsma, and S Van der Zwaag. Three-dimensional phase field modelling of the austenite-to-ferrite transformation. *Acta materialia*, 54(15):3961–3972, 2006.

[57] C. Capdevila, J. Cornide, K. Tanaka, K. Nakanishi, and E. Urones-Garrote. Kinetic Transition during Ferrite Growth in Fe-C-Mn Medium Carbon Steel. *Metallurgical and Materials Transactions A*, 42(12):3719–3728, December 2011.

[58] H.P. Van Landeghem, B. Langelier, B. Gault, D. Panahi, A. Korinek, G.R. Purdy, and H.S. Zurob. Investigation of solute/interphase interaction during ferrite growth. *Acta Materialia*, 124:536–543, February 2017.

[59] F. Danoix, X. Sauvage, D. Huin, L. Germain, and M. Gouné. A direct evidence of solute interactions with a moving ferrite/austenite interface in a model Fe-C-Mn alloy. *Scripta Materialia*, 121:61–65, August 2016.

[60] M Guttmann. Equilibrium segregation in a ternary solution: A model for temper embrittlement. *Surface Science*, 53(1):213–227, 1975.

[61] M Enomoto, CL White, and HI Aaronson. Evaluation of the effects of segregation on austenite grain boundary energy in fe-cx alloys. *Metallurgical Transactions A*, 19(7):1807–1818, 1988.

[62] H. P. Van Landeghem, B. Langelier, D. Panahi, G. R. Purdy, C. R. Hutchinson, G. A. Botton, and H. S. Zurob. Solute Segregation During Ferrite Growth: Solute/Interphase and Substitutional/Interstitial Interactions. *JOM*, 68(5):1329–1334, May 2016.

## Supplementary material

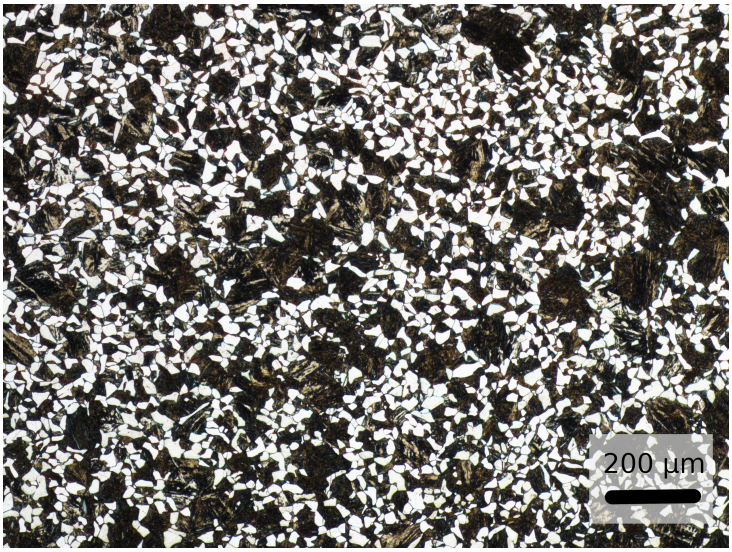


Figure S1: Micrograph showing microstructure of a Fe-C-Ni sample transformed at 750 °C for 30s. It can be shown that ferrite is formed along the austenite grain boudaries during the early stages of the transformation indicating nucleation site saturation.

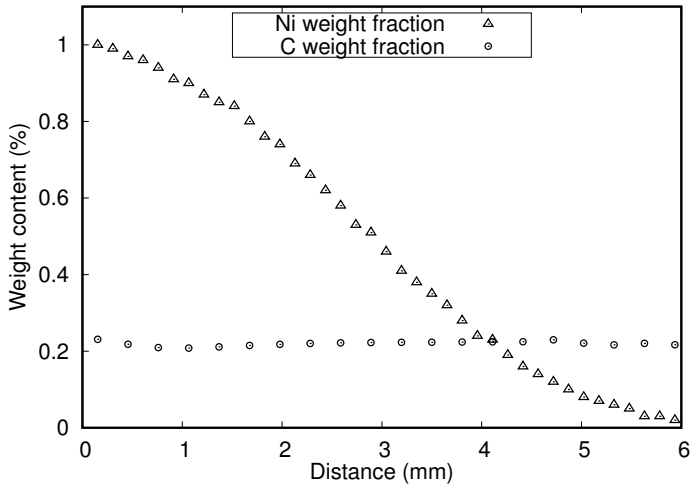


Figure S2: Measured composition profiles using electron probe micro-analysis across Fe-C/Fe-C-Ni diffusion couple.

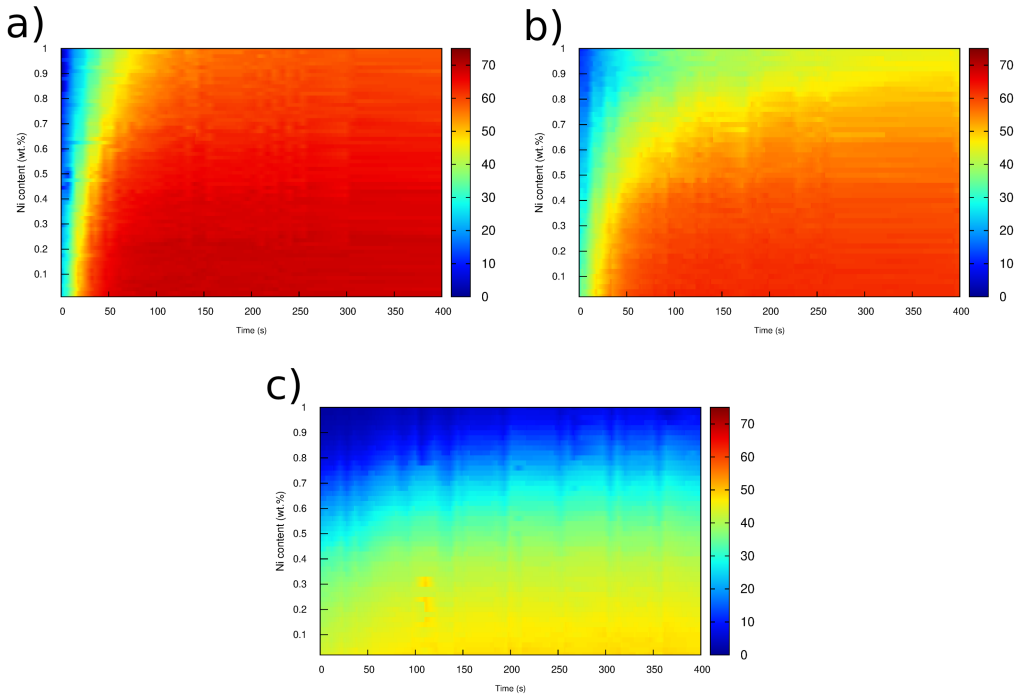


Figure S3: Heat maps illustrating ferrite volume fraction evolution as a function of time and nickel composition at : a) 730°C, b) 750°C and c)775°C.

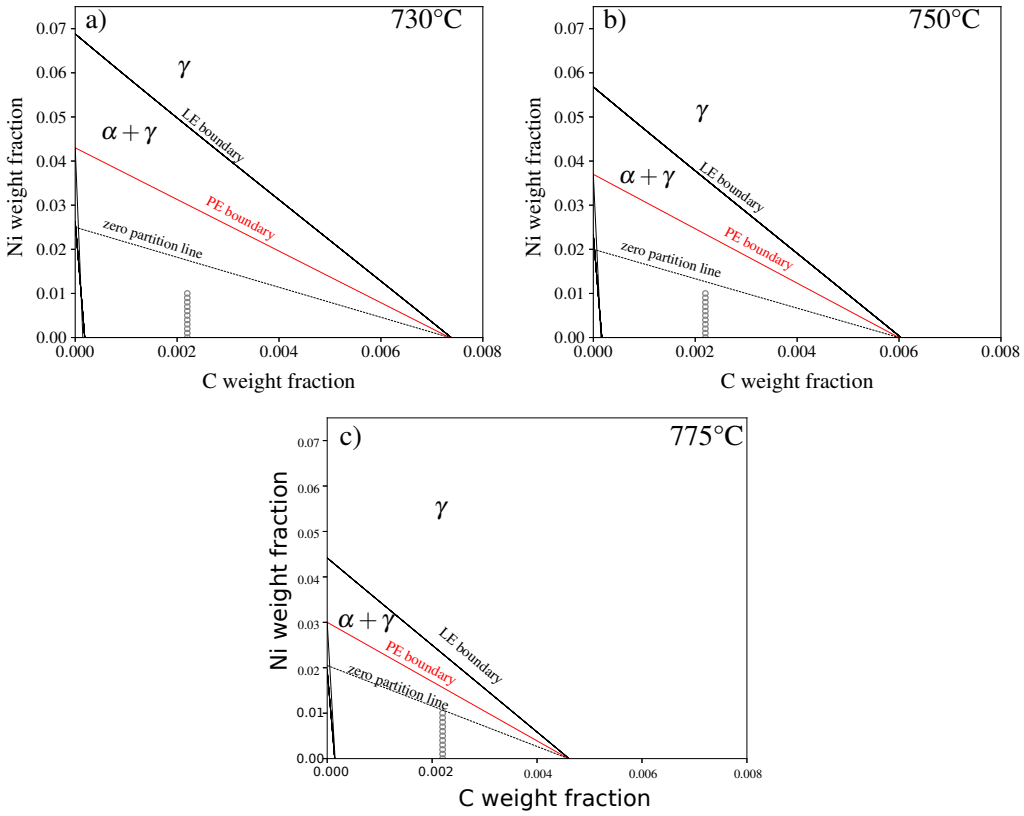


Figure S4: Isothermal sections of the Fe-C-Ni phase diagram at : a) 730°C, b) 750°C and c)775°C, showing the different growth modes (LEP-LENP and PE) for the composition range of the Fe-C-Ni diffusion couple (gray circles).

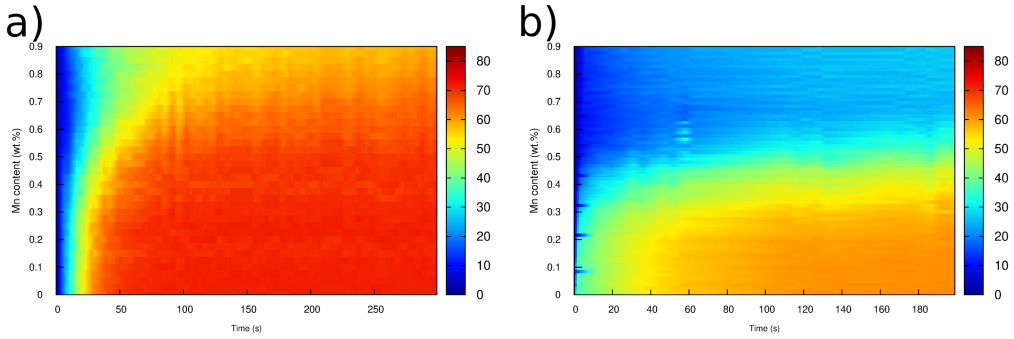


Figure S5: Heat maps illustrating ferrite volume fraction evolution as a function of time and manganese composition at : a) 730°C and b) 750°C.

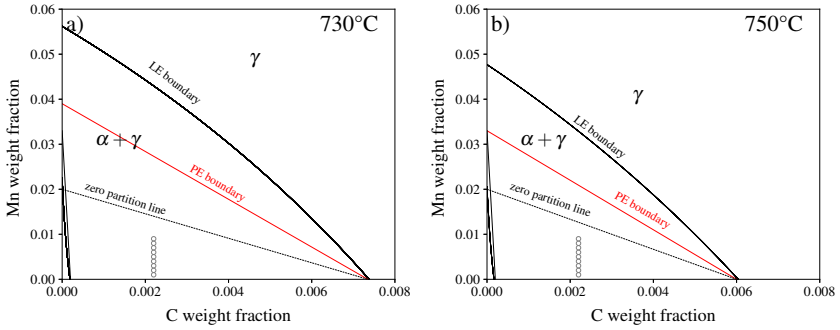


Figure S6: Isothermal sections of the Fe-C-Mn phase diagram showing the gradient of manganese composition of the diffusion couple (gray circles) at : a) 730°C and b) 750°C.

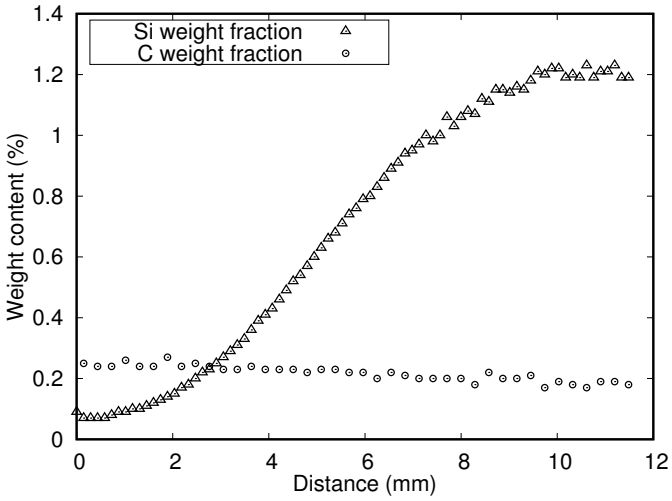


Figure S7: Measured composition profiles using electron probe micro-analysis across Fe-C/Fe-C-Si diffusion couple.

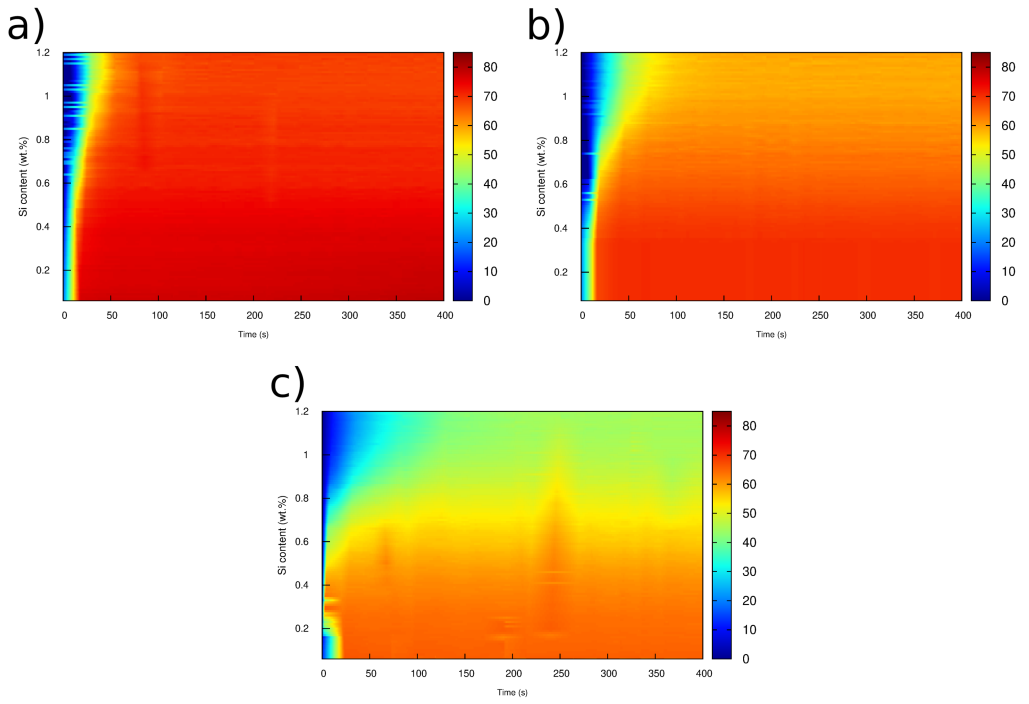


Figure S8: Heat maps illustrating ferrite volume fraction evolution as a function of time and silicon composition at : a) 730°C, b) 750°C and c) 775°C.

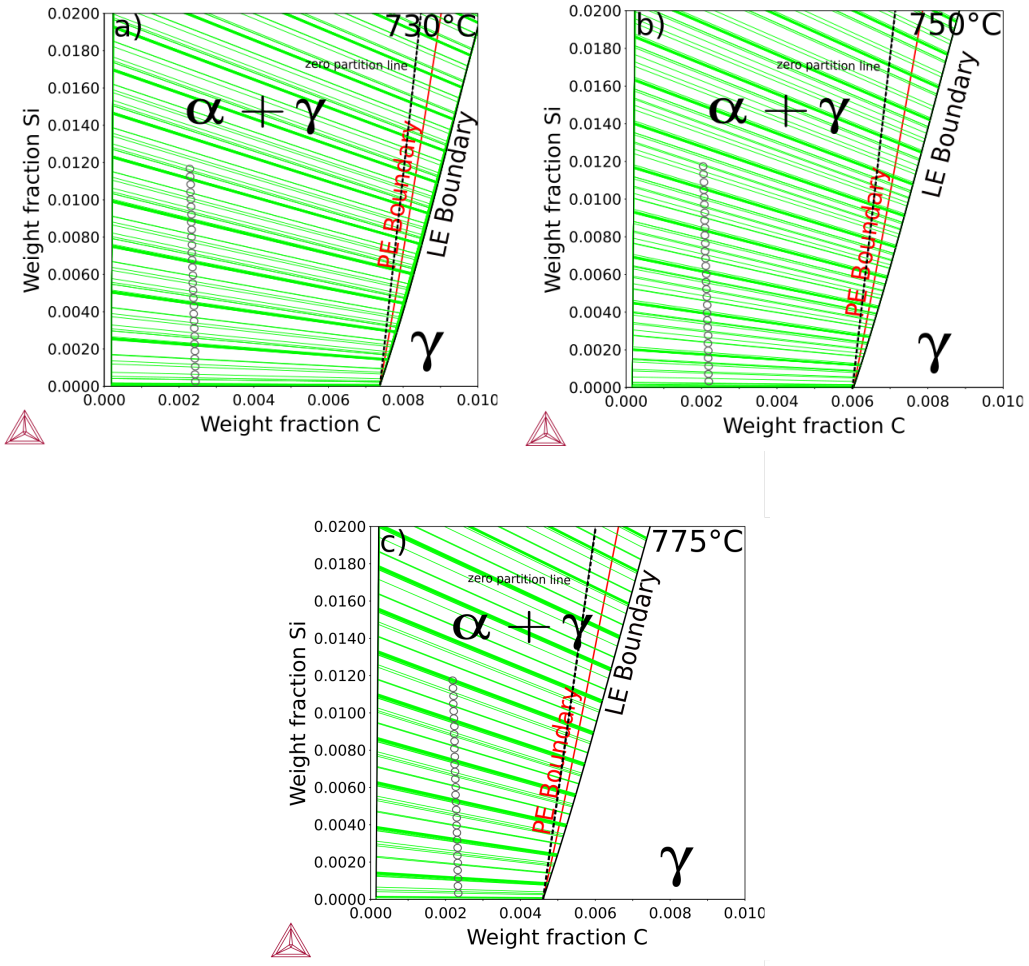


Figure S9: Isothermal sections of the Fe-C-Si phase diagram showing the gradient of composition of the diffusion couple Fe-C/Fe-C-Si (gray circles) at : a) 730°C, b) 750°C and c 780°C.The equilibrium tie-lines of the two phase field are shown in green.

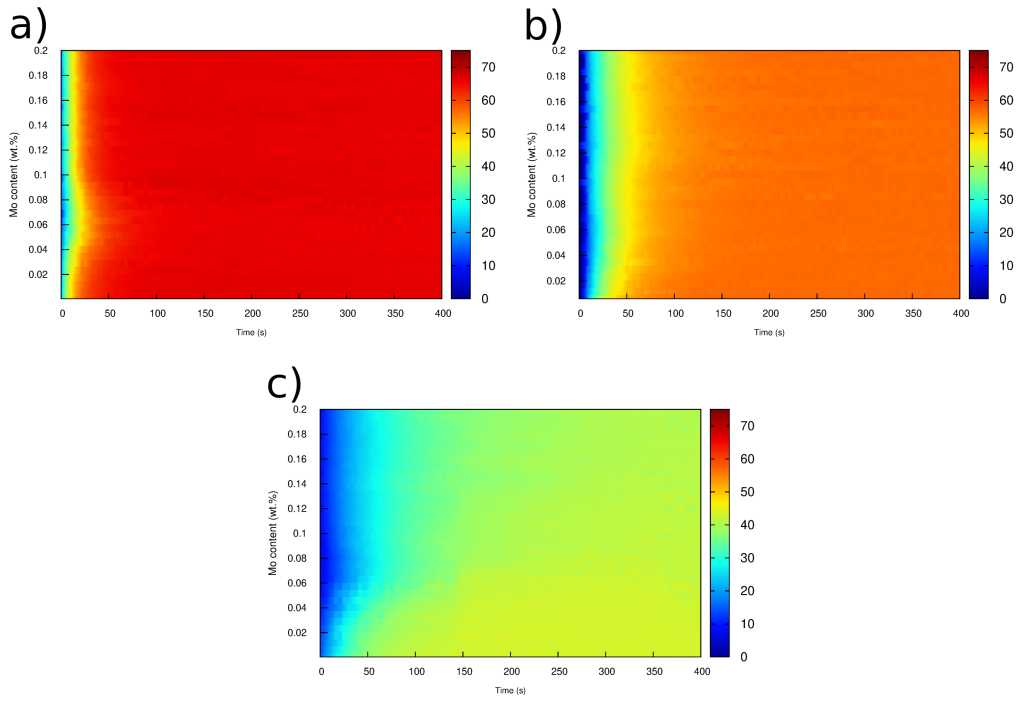


Figure S10: Heat maps illustrating ferrite volume fraction evolution as a function of time and molybdenum composition at : a) 730°C, b) 750°C and c) 780°C.

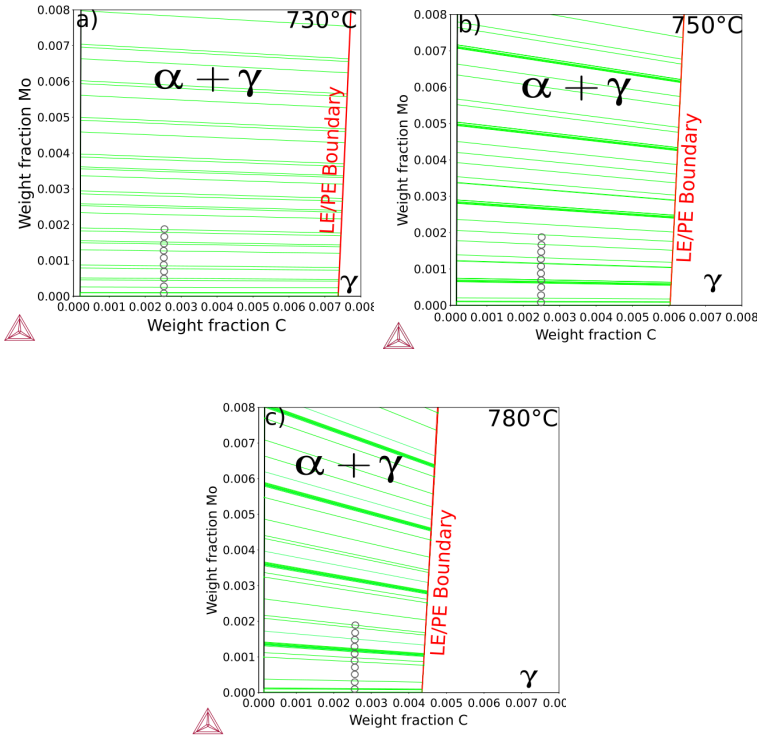


Figure S11: Isothermal sections of the Fe-C-Mo phase diagram showing the gradient of composition of the diffusion couple (gray circles) at : a) 730°C, b) 750°C and c 780°C. The equilibrium tie-lines of the two phase field shown in green are almost horizontal making the predicted kinetics using local equilibrium with negligible partitioning and paraequilibrium identical.

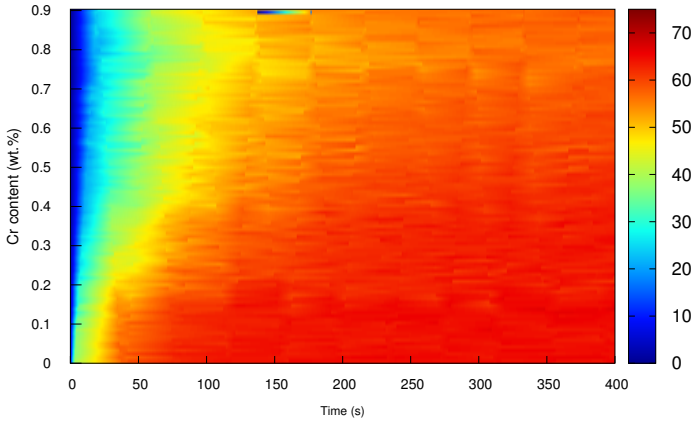


Figure S12: Heat maps illustrating ferrite volume fraction evolution as a function of time and chromium composition at 750°C.

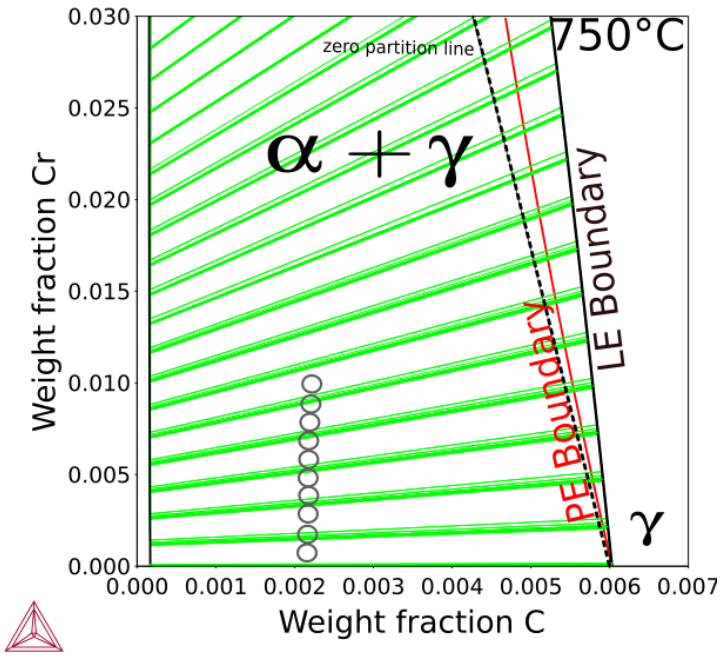


Figure S13: Isothermal sections of the Fe-C-Cr phase diagram showing the gradient of composition of the diffusion couple (gray circles) at 730°C. The equilibrium tie-lines of the two phase field are shown in green.

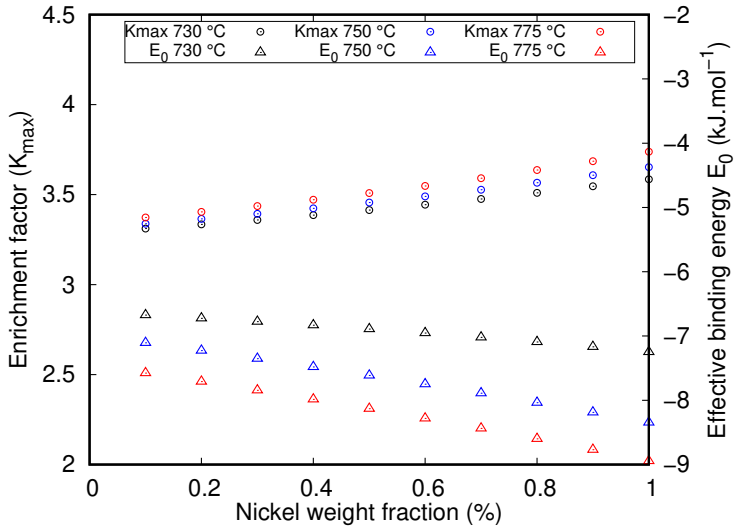


Figure S14: The enrichment factor $K_{max}$ and the corresponding effective binding energy ($E_0$) evolution as a function of nickel content for the three temperatures, 730°C, 750°C and 775°C.

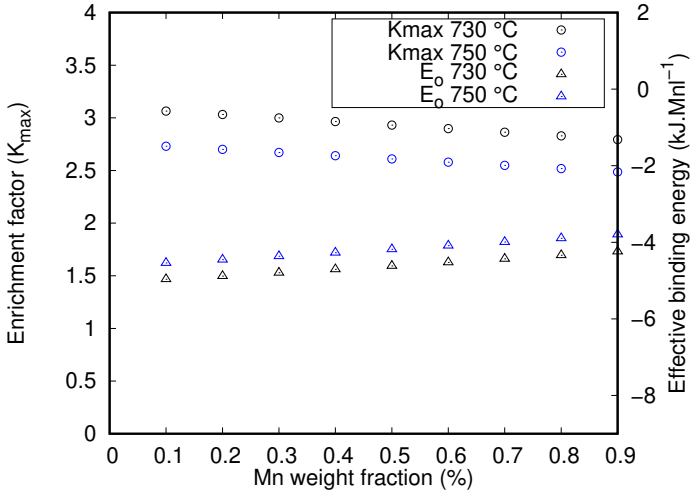


Figure S15: Evolution of the enrichment factor $K_{max}$ (a) and the corresponding effective binding energy ($E_0$) (b) as a function of manganese content for the two temperatures, 730°C and 750°C.

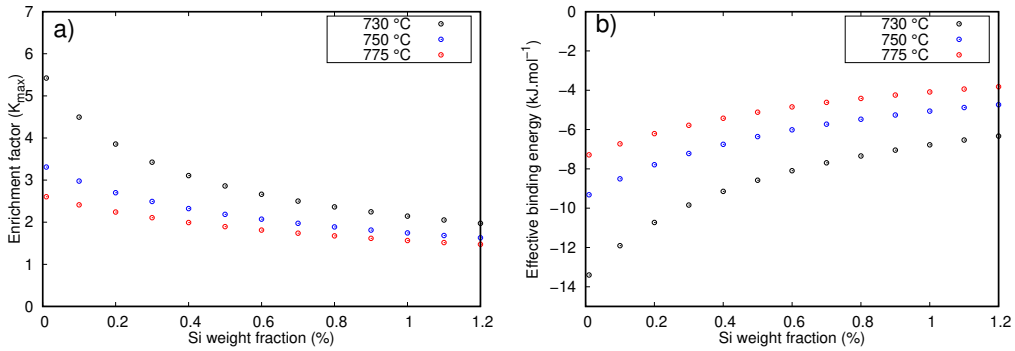


Figure S16: a) Enrichment factor $K_{max}$ and b)the corresponding effective binding energy ($E_0$) evolution as a function of silicon content for the two temperatures, 730°C, 750°C and 775°C.

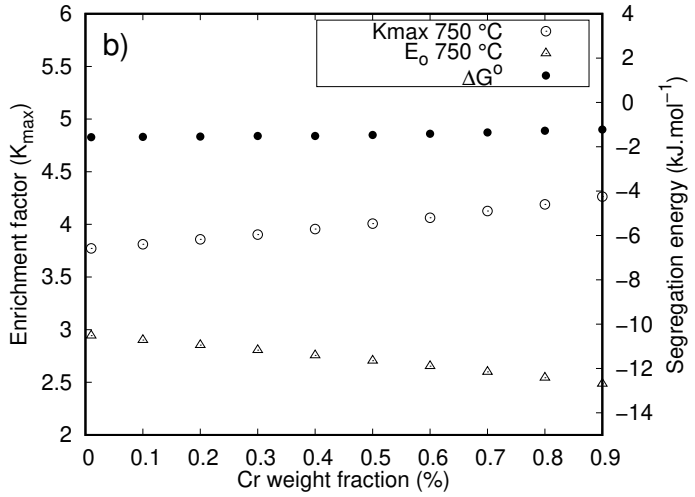


Figure S17: Evolution of the enrichment factor $K_{max}$ and the corresponding effective binding energy ($E_0$) as a function of chromium content at 750°C. The intrinsic segregation energy of chromium is also shown.